



学汇百川 德济四海

# 科研绘图经验分享

姓名：刘翔宇

导师：潘新祥教授 徐敏义教授

2022年4月1日



「01」 论文图片绘制

「02」 汇报PPT绘制

「03」 总结与心得



# 如何选择合适的字体

## 1.选用sans serif (无衬线) 字体

- 首选：Arial , Helvetica , 微软雅黑
- Adobe : Myriad
- Apple : San Francisco

## 2.字号要小

- 5pt — 7pt

## 3.尽量不添加颜色

## 4.尽量不加斜体

## 5.数量-单位/运算符之间加空格

- $10\mu W \rightarrow 10 \mu W$

AaBbCc Sans-serif font  
AaBbCc Serif font  
AaBbCc Serif font (red serifs)

**nature**

Explore content ▾ About the journal ▾ Publish with us ▾ Subscribe

View all journals Search Q Login @

Sign up for alerts RSS feed

nature > for authors > final submission

For Authors

- Editorial criteria and processes
- Formatting guide
- Presubmission enquiries
- Initial submission
- Final submission
- Supplementary information
- Forms and declarations
- Matters Arising
- Other types of submissions
- Publishing options

**Final submission**

This guide provides information on preparing production-quality figures and text files. The instructions apply only if your manuscript has been accepted in principle for publication and an editor has asked you to upload production-quality material.

**General information**

Before your manuscript can be formally accepted for publication and passed to our subediting, art and production departments, you will need to upload electronic files of your text, figures, Extended Data figures and tables, and Supplementary Information (if any) to our server. You will also need to upload scanned copies of any forms and declarations requested by the editorial office for signing (these may be faxed if scanning is not possible, with the fax labelled clearly with the corresponding author name and manuscript reference number).

Please follow these guidelines to ensure that your final files are complete and in the correct format. This will speed the handling of your manuscript after it is accepted, reduce delays and minimize potential errors.

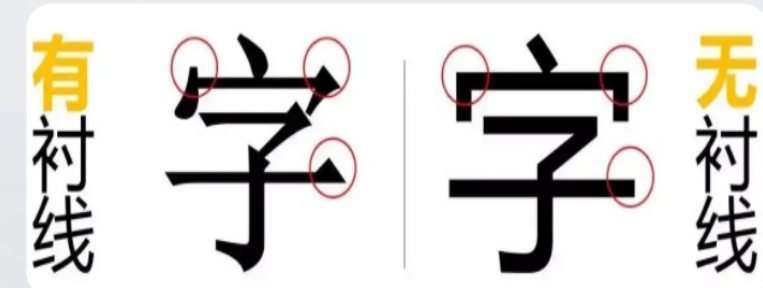
If you are unable to upload production-quality files to our server, you should contact *Nature*'s London office for details of how files may be sent on disk, although you should be aware that online submission is the preferred route and submission by other means may delay acceptance and/or publication of your paper.

**Lettering**

Lettering should be in a sans-serif typeface, preferably Helvetica or Arial, the same font throughout all figures in the paper. Units, capitalization, etc. should follow *Nature* style. Where practical, avoid placing lettering directly over images or shaded areas.

Separate panels in multi-part figures should each be labelled with 8 pt bold, upright (not italic) a, b, c. Maximum text size for all other text should be 7 pt; minimum text size should be 5 pt. Amino-acid sequences should be presented in one-letter code in Courier.

Do not rasterize or convert text to outlines.



**ACS Publications**  
Most Trusted. Most Cited. Most Read.

**ACS NANO**

**ACS Nano Author Checklist**

Before submitting your revised manuscript, please ensure the following guidelines are met:

**Copyrights and Permissions:**

- Provide letter or email from author(s) of personal communications granting you permission to cite unpublished work. We do not list references as submitted for publication, in preparation, etc.; if not in the press, these should be listed within the text (not in the reference list) as personal communications or unpublished data, if from an author of the present manuscript.
- Provide permission obtained to reproduce previously published (copyrighted) material.
- No institutional logos are allowed in graphic files without explicit permission.

**Table of contents graphic:**

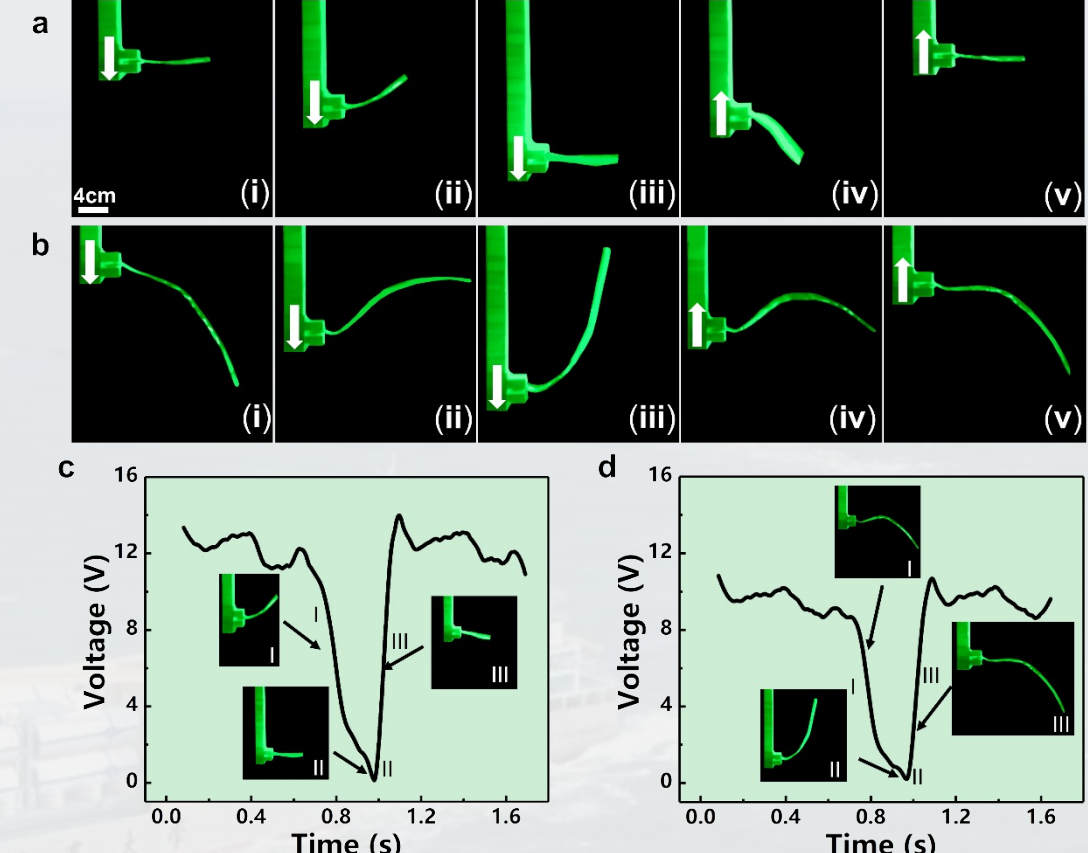
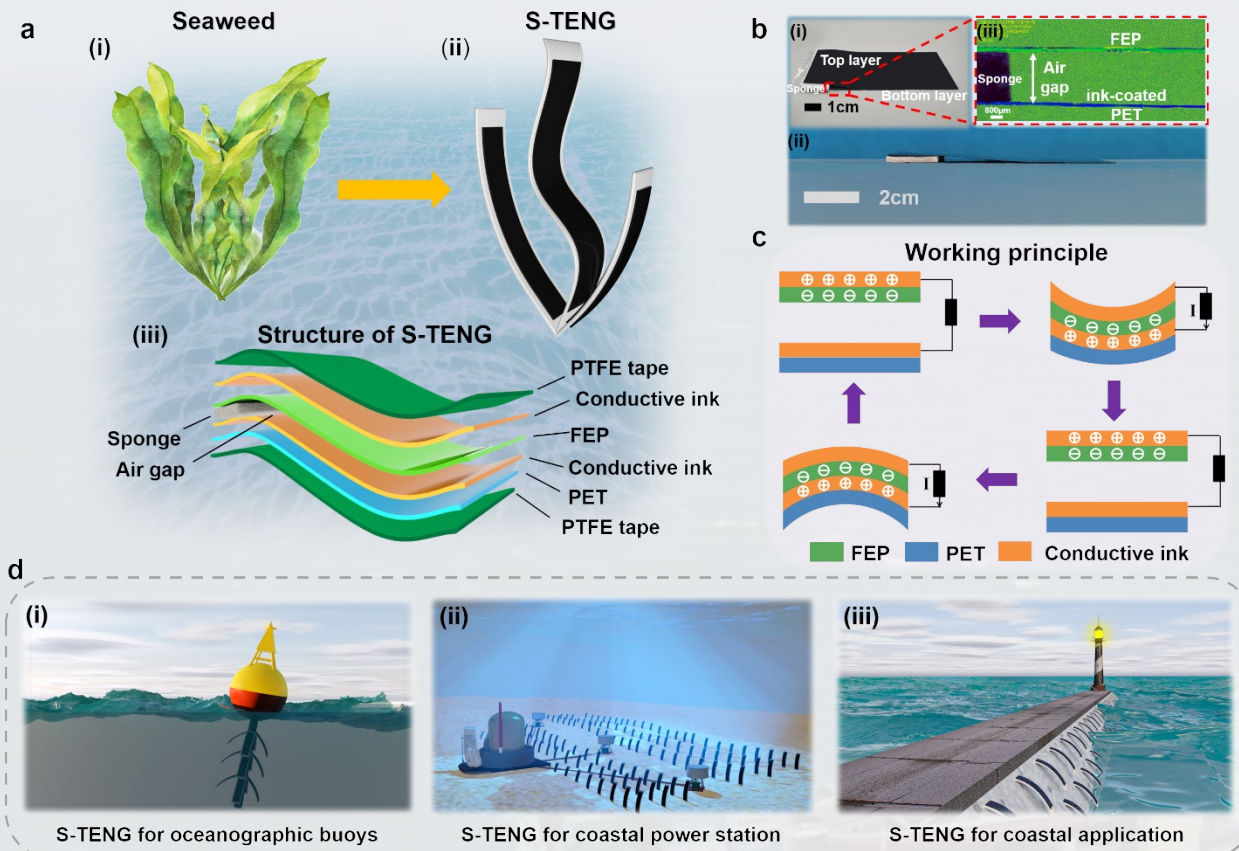
- All Table of Contents (TOC) images must be original, created by one of the authors, and cannot be reproduced, adapted, or modified from other sources. Images modified through manipulation including rearranging, cropping, masking, and distorting, should not be used. The use of licensed stock images in TOC graphics is not allowed.
- TOC graphic is required for the following manuscript types: Articles and Reviews, maximum width 9.0 cm and height 4.0 cm; Perspective and Nano Focus, maximum width 4.5 cm and height 4.0 cm. This graphic should be in TIF or EPS format and at least 300 dpi resolution at final printed size. The graphic should capture the readers' attention and provide a visual impression of the essence of the manuscript. Please keep the text portion of the image to a minimum. Consult the [Guidelines for Table of Contents/Abstract Graphics for specifications](#).
- Under no circumstance can a logo be included in the TOC graphic.

**Figures and tables:**

- All figures and tables must be cited in order (e.g., Figure 1A).
- Figures must have captions.
- Schemes must have titles and may contain footnotes.
- Structures should be numbered with boldface Arabic numbers.
- Use **Arial** for lettering within a graphic. Lettering should be of uniform size and density, points and lines should be no thinner than 0.5 point at final published size.
- Figures containing photographic images must be at least 300 dpi TIF files in RGB format; should be at least 1200 dpi EPS files.
- Figures must be submitted at final published size.



# 如何选择合适的字体



1. 字体：序号、文字标注始终保持一致（无衬线字体）
2. 字号：序号、文字标注的字号保持一致，序号 > 标注
3. 非必要情况，尽量不改变颜色、不使用斜体



# 论文示意图的绘制

## 1.模型建立/绘制

- Solidworks/CAD
- Cgmodel.com
- Cg99.com

## 2.软件渲染上色

- Cinema 4D
- 3dmax/Maya
- Keyshot

## 3.成图后处理

- PS/AI/AE
- 导出Tif/Tiff格式



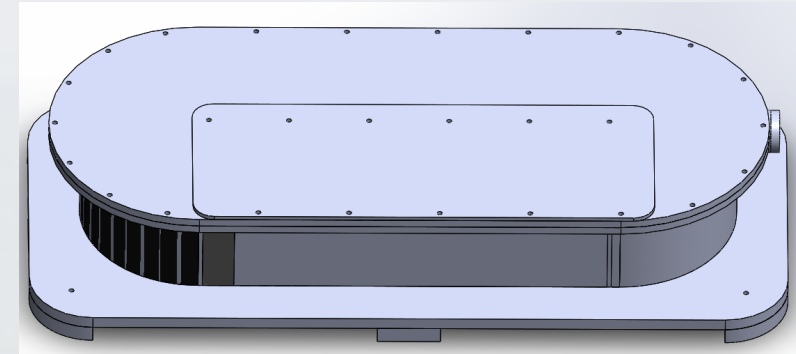
模型元素：ROV、贝壳、珊瑚、礁石



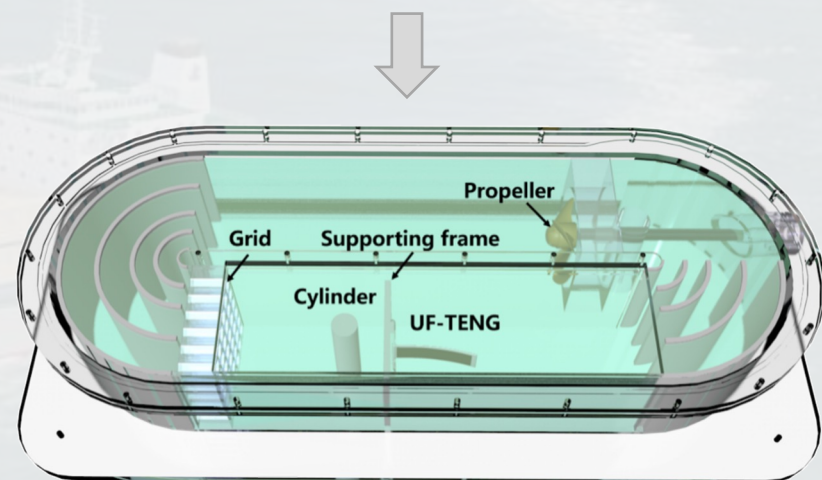
C4D中海底场景、灯光元素的建立



渲染、PS后处理（调亮度、饱和度）



模型元素：循环水槽



材质的选择、渲染、后处理

保持美观 浅显易懂



# C4D工作窗口

## 1.渲染器

- 自带标准渲染器
- Octane渲染器

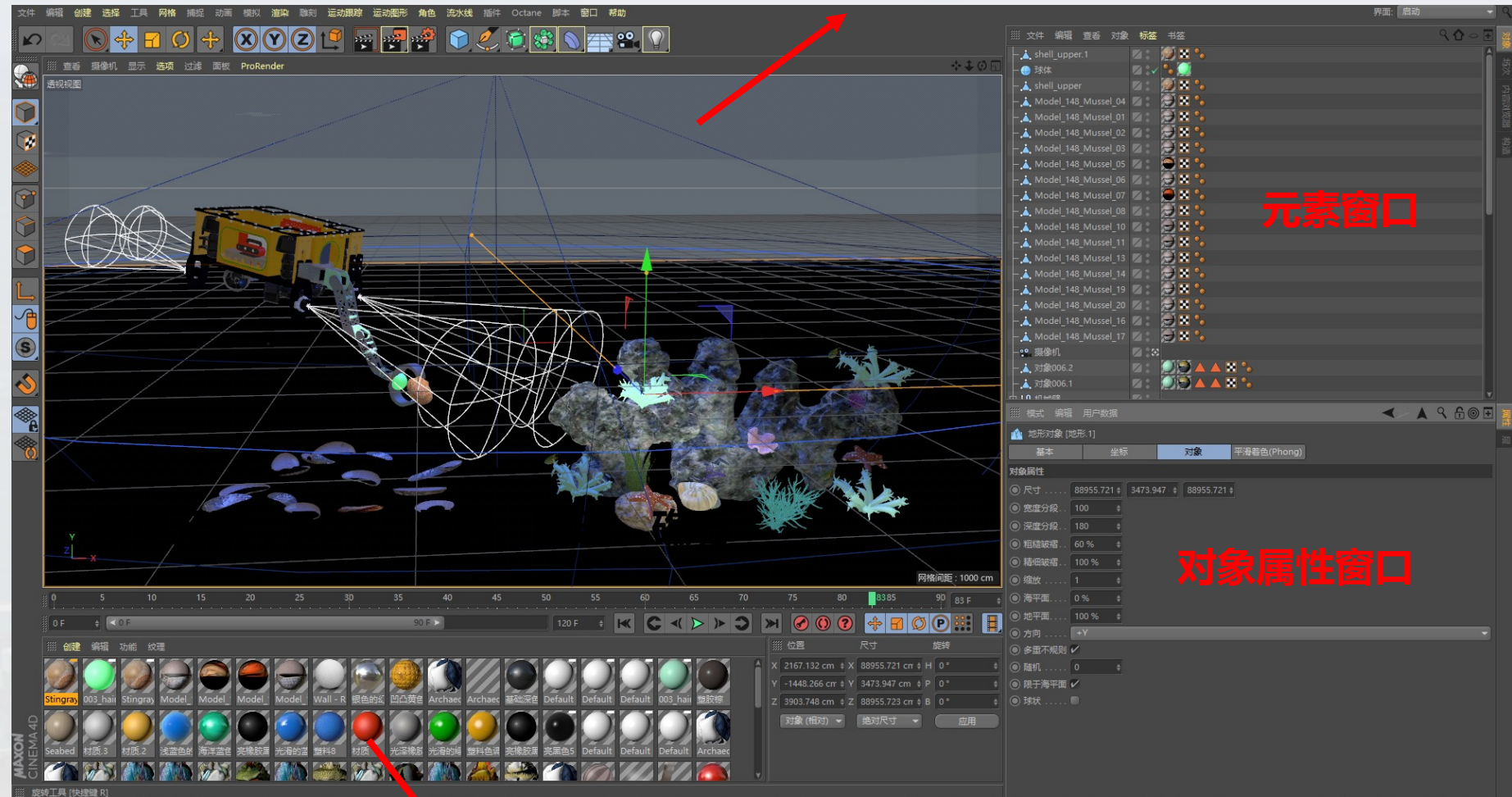
## 2.材质球的选择

- 现有材质包
- 自调材质包

## 3.插件选择

- 海洋插件
- 粒子插件

.....



材质球窗口

元素窗口

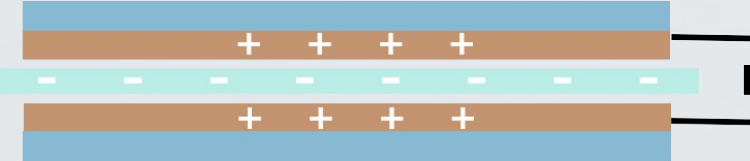
对象属性窗口

工作窗口/预渲染窗口

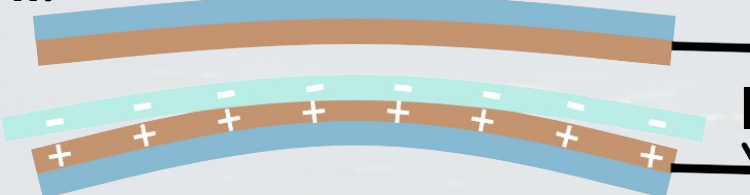


# PPT绘制

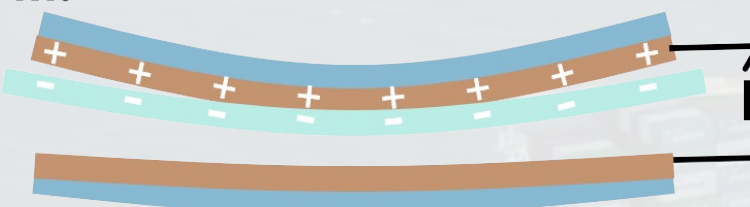
d. i.



ii.



iii.



嗨！同学，PPT绘制的光路示意图来了！！！

纳米发电机 2022-03-31 17:15

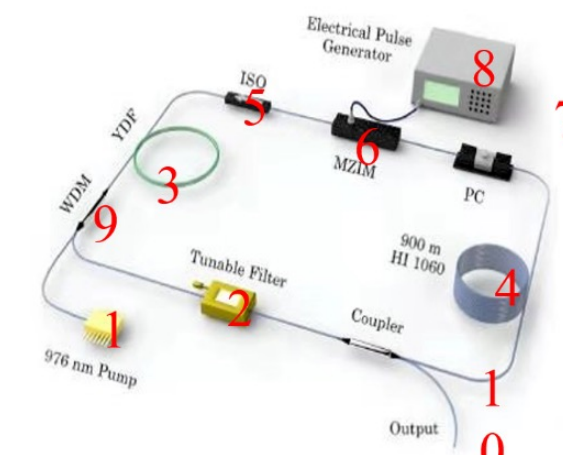
以下文章来源于伊曼如歌，作者七月sun



伊曼如歌

科研人的知识加油站！

>



【PPT特辑·C60分子结构绘制】

原创 零尘世 零尘世 2020-06-11 11:27

收录于话题

#PPT科研绘图-补位专辑

12个 >

C60是一种结构高度对称的分子，由32个面组成，12个正五边形、20个正六边形，这就意味着PPT画出其3D结构可以大概率实现。笔者以前考虑过全3D无死角的画法，但考虑到后期计算量（人脑&PPT）巨大，最后不得不放弃。

简要思路：正六边形+球的基本单元、正五边形+球的基本单元，利用补位手法迅速绘制与这些基本单元对称的结构。两个基本单元的属性要求：尺寸大小一样、旋转中心一样、是运用补位原理构建的组合。

考虑到教程长度，以下内容中基本操作（如设置棱台、距底边高度、调出选择窗口、水平翻转等）均不再详细列出，只给出具体参数。PPT里用到的部分插件，本号后台回复“PPT插件”可以获得相关信息。

正文如下：

①绘制正六边形+球体的基本单元

利用英豪插件“添加正多边形”功能绘制一个正六边形，右键属性锁定纵横比，宽度修改为4cm，无填充，线条浅灰色、宽度10磅。

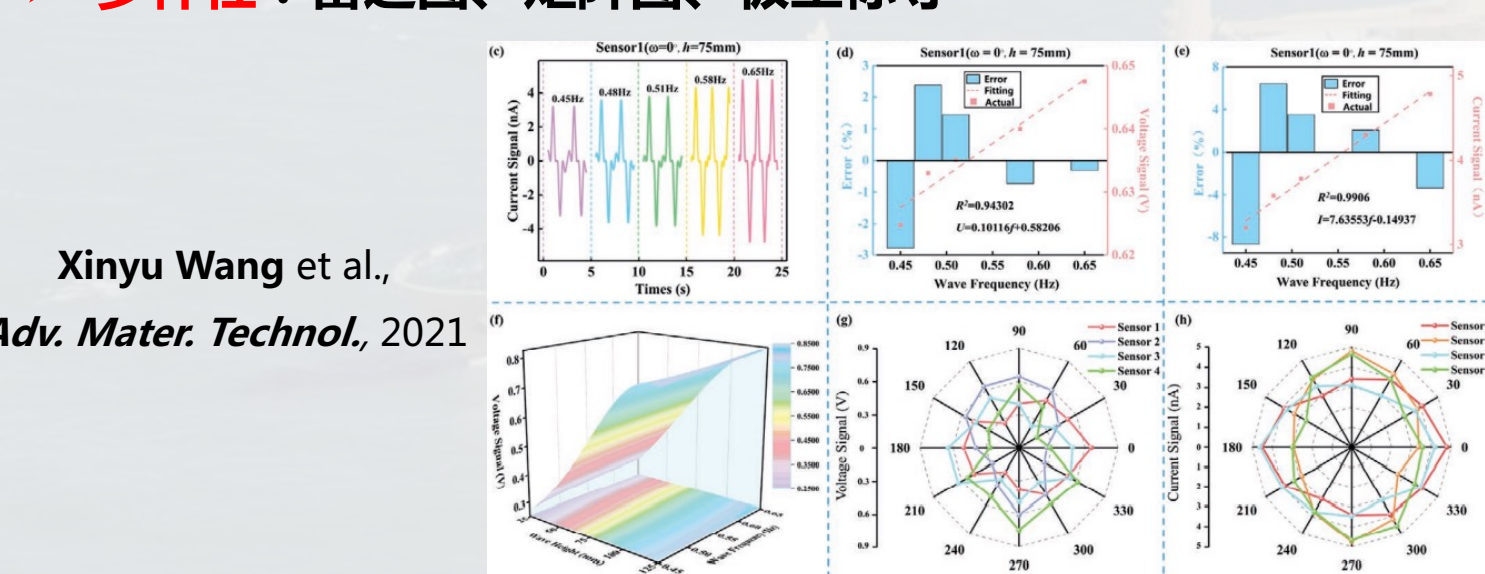


形状格式的调整、插件的选择等  
自学平台：B站、公众号等

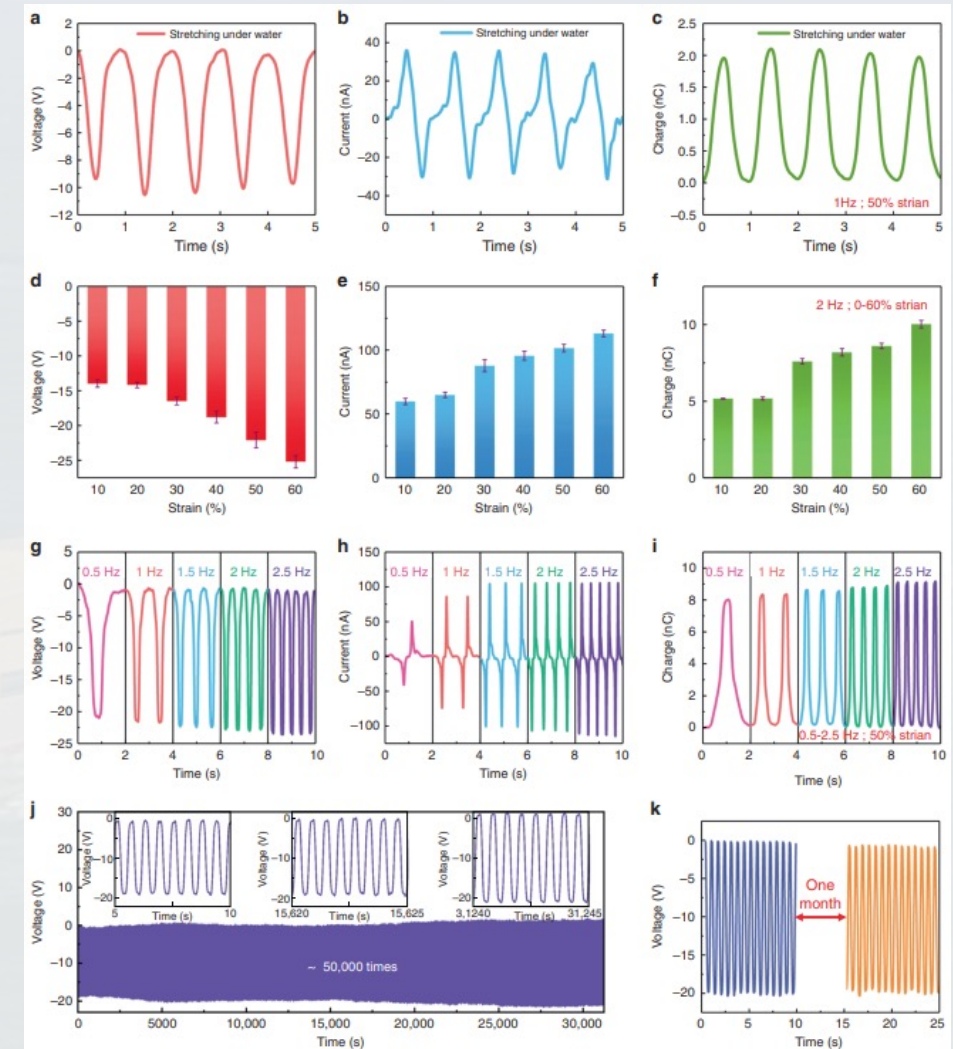


# 论文数据图的绘制

- Origin作图长宽比一般为**1:1**，便于和其他图片拼合
- 坐标轴的主刻度尺朝内，图片高度3-4 cm, 字号8 pt
- 坐标轴0.5或0.75 pt，曲线线条0.75或1 pt
- 推荐Origin输出Tiff图在PPT中做后期，图片文字大小、线条粗细**保持一致**
- 对多个变量合理使用渐变色，会使逻辑更加清楚
- **多样性**：雷达图、矩阵图、极坐标等



Xinyu Wang et al.,  
Adv. Mater. Technol., 2021



Zhou Li et al., Nature communication, 2019



# 论文toc图的制作

ACS NANO

www.acsnano.org

## Artificial Intelligence of Things (AIoT) Enabled Floor Monitoring System for Smart Home Applications

Qiongfeng Shi, Zixuan Zhang, Yanqin Yang, Xuechuan Shan, Budiman Salam, and Chengkuo Lee\*

Cite This: <https://doi.org/10.1021/acsnano.1c07579>

Read Online

ACCESS | Metrics & More

Article Recommendations

Supporting Information

**ABSTRACT:** To enable smart homes and relative applications, the floor monitoring system with embedded triboelectric sensors has been proven as an effective paradigm to capture the ample sensory information from our daily activities, without the camera-associated privacy concerns. Yet the inherent limitations of triboelectric sensors such as high susceptibility to humidity and long-term stability remain a great challenge to develop a reliable floor monitoring system. Here we develop a robust and smart floor monitoring system through the synergistic integration of highly reliable triboelectric coding mats and deep-learning-assisted data analytics. Two quaternary coding electrodes are configured, and their outputs are normalized with respect to a reference electrode, leading to highly stable detection that is not affected by the ambient parameters and operation manners. Besides, due to the universal electrode pattern design, all the floor mats can be screen-printed with only one mask, rendering higher facileness and cost-effectiveness. Then a distinctive coding can be implemented to each floor mat through external wiring, which permits the parallel-array connection to minimize the output terminals and system complexity. Further integrating with deep-learning-assisted data analytics, a smart floor monitoring system is realized for various smart home monitoring and interactions, including position/trajetory tracking, identity recognition, and automatic controls. Hence, the developed low-cost, large-area, reliable, and smart floor monitoring system shows a promising advancement of floor sensing technology in smart home applications.

**KEYWORDS:** floor monitoring, artificial intelligence, deep learning, triboelectric nanogenerator, smart home, coding



Chengkuo Lee et al., *ACS nano*, 2021

保持美观 保证凝练

## Toc : Table of content/Graphical Abstract

### Specifications

- The graphic should be in the form of a structure, graph, drawing, photograph, or scheme—or a combination.
- Text should usually be limited to the labeling of compounds, reaction arrows, and diagrams. Long phrases or sentences should be avoided.
- Submit the graphic at the actual size to be used for the TOC so that it will fit in an area no larger than 3.25 inches by 1.75 inches (approx. 8.25 cm by 4.45 cm).
- Use a sans serif font type such as Helvetica, preferably at 8 pt. but no smaller than 6 pt. Do not make the reader strain to read it. The type should be of high quality in order to reproduce well.
- The graphic file should be saved as either:
  - TIFF at 300 dpi for color and at 1200 dpi for black and white.
  - EPS in RGB document color mode with all fonts converted to outlines or embedded in the file.
- Label the graphic "For Table of Contents Only" and provide it on the last page of the submitted manuscript.



长度不超  
8.25cm

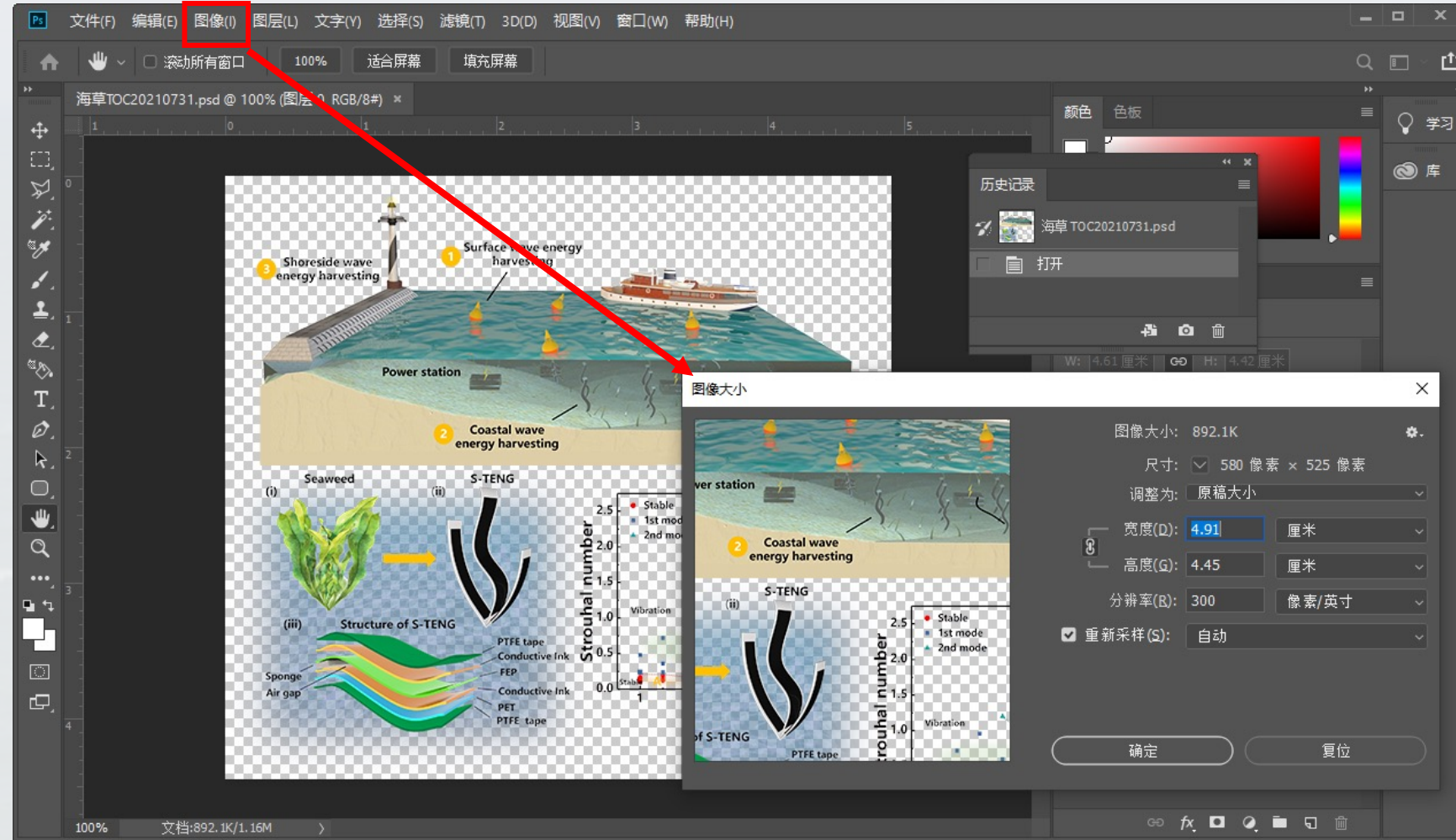
宽度不超

4.45cm

300DPI



# 论文toc图的制作—PS工作窗口



**注意：若Toc里有文字说明，请在处理完图片后在PPT上另加文字  
否则图像缩小后文字将变得模糊！**



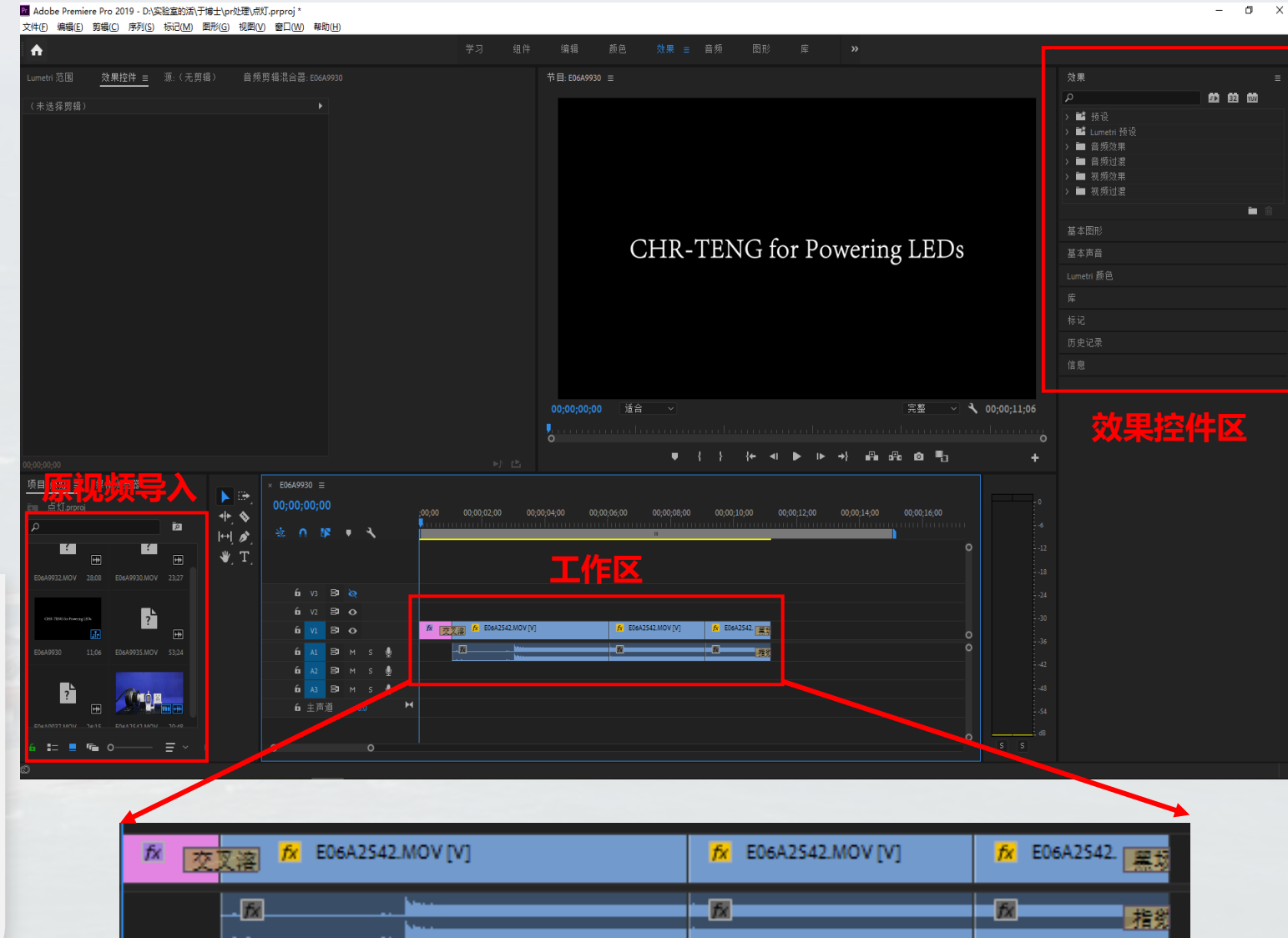
# 论文demo的制作—Pr工作窗口

CHR-TENG for Powering a Theremometer

Haichao Yuan et al., *Nanomaterials*, 2021

## Tips

1. 原视频录制过程中保持无环境杂音
2. 保持录制设备的固定/稳定运镜
3. 导出**中等比特率**，文件大小20M以内
4. Pr2021兼容苹果手机拍照视频



插入字幕、关键帧、转场等元素效果



# 论文大图的绘制

1

科研论文配图的演变

2

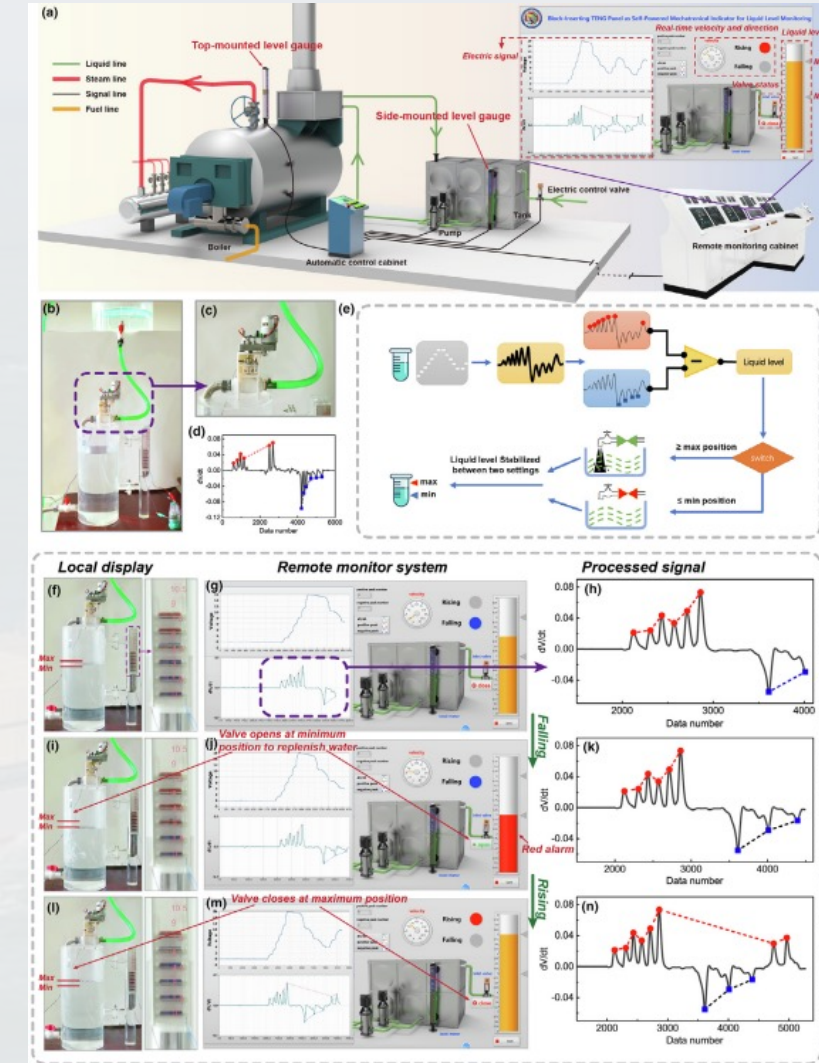
科研论文配图的建议

3

常用色彩搭配网址

4

大图的构思与排版



Minyi Xu\* et al., *Materials Today*, 2021



# 科研论文配图的演变

## 1. 90年之前：

- 黑白灰的世界，图少数据少彩色少

## 2. 90-00年：

- 彩色图开始兴起，少数杂志要求彩色图

## 3. 00-10年：

- 数据量增大、SI增加，彩色比重加大

## 4. 10-20年：

- 强调效果与模型、3D透視效果图运用增加

## 5. 未来：

- 虚拟现实人机交互（动画）

## Nature, 1989

If the Fermi-liquid states were supplied by the BiO plane, which is the case for the Cu<sub>2</sub>O<sub>3</sub> plane, then the same mechanism based on the Fermi-liquid states would also apply to the Cu<sub>2</sub>O<sub>3</sub> plane. Scanning tunnelling spectroscopy (STS), combined with photoemission (PES) and inverse photoemission (IPES) spectroscopies, which show the electronic structure of the Cu<sub>2</sub>O<sub>3</sub> plane, indicate that the Cu<sub>2</sub>O<sub>3</sub> plane forms the Fermi liquid state.

It has been suggested that one may prevent the 1/2 O<sub>2</sub> band across the Fermi energy from giving a substantial density of states at  $E_F$ . Although photoemission studies<sup>12</sup> have shown that the Fermi energy lies in the Cu<sub>2</sub>O<sub>3</sub> plane, the nature of the Fermi-edge states is controversial; they have been assigned by some to the BiO plane<sup>13</sup> and by others to the Cu<sub>2</sub>O<sub>3</sub> plane<sup>14</sup>. We have performed 3D measurements on single-crystal Bi<sub>2</sub>Cu<sub>3</sub>O<sub>6</sub> using scanning tunnelling microscopy (STM)<sup>15</sup>, which has been developed to study the surface electronic structure. The technique has proved to be useful for high-energy-resolution studies of the electronic structure of the uppermost atomic layer of a solid surface.

We used a single crystal of Bi<sub>2</sub>Cu<sub>3</sub>O<sub>6</sub> (of dimensions 5 × 5 × 1 mm<sup>3</sup>) and found that the surface of the crystal has a smooth plane along which cleavage is easy. A magnetic-susceptibility measurement showed that the crystal becomes superconducting at 6.5 K. The sample was cleaved under the STM/STS spectrometer and was kept at room temperature under ultra-high vacuum ( $\sim 10^{-10}$  torr) during measurements. The details of our STM/STS experiments and data processing procedures have been described elsewhere<sup>15</sup>. We obtained a large-area STM image (Fig. 1a) and two spectra (Fig. 1b, c) from the same area (Fig. 1); these rows correspond to the incommensurate superstructure along the  $\langle 11\bar{2}\rangle$  direction of the crystal. The fact that the same incommensurate superstructure appears on the cleaved surface of the Bi<sub>2</sub>Cu<sub>3</sub>O<sub>6</sub> single crystal suggests weak interlayer interaction between BiO planes in bulk. Thus one would expect little difference between the electronic structure of a BiO plane on a surface, as probed by STS, and that of a BiO plane in bulk.

Figure 2 shows representative  $I-V$  and conductivity ( $dI/dV$ ) curves measured on a cleaved surface of a Bi<sub>2</sub>Cu<sub>3</sub>O<sub>6</sub> single crystal. In a current of 1 mA, a sample bias of -0.5 V and a scanning area of 23 × 23 nm<sup>2</sup>, the  $I-V$  curve shows two steps corresponding to the superstructure. The  $dI/dV$  spectrum shows a sharp peak at the Fermi level ( $E_F$ ). The normalized conductivity curve ( $|dI/dV|/|V|$ ) obtained from the  $I-V$  curve shows a broad peak at the Fermi level. This broad peak, however, Martensson and Feenstra<sup>16</sup> found, that for a large surface band gap, calculations of the normalized conductivity

become zero near the Fermi level.

Figure 3 shows the  $I-V$  and conductivity ( $dI/dV$ ) curves of a cleaved surface of Bi<sub>2</sub>Cu<sub>3</sub>O<sub>6</sub>.

Figure 2 The  $I-V$  and conductivity ( $dI/dV$ ) curves of a cleaved surface of Bi<sub>2</sub>Cu<sub>3</sub>O<sub>6</sub>.

Figure 3 The  $I-V$  and conductivity ( $dI/dV$ ) curves of a cleaved surface of Bi<sub>2</sub>Cu<sub>3</sub>O<sub>6</sub>.

Figure 4 The  $I-V$  and conductivity ( $dI/dV$ ) curves of a cleaved surface of Bi<sub>2</sub>Cu<sub>3</sub>O<sub>6</sub>.

Figure 5 The  $I-V$  and conductivity ( $dI/dV$ ) curves of a cleaved surface of Bi<sub>2</sub>Cu<sub>3</sub>O<sub>6</sub>.

Figure 6 The  $I-V$  and conductivity ( $dI/dV$ ) curves of a cleaved surface of Bi<sub>2</sub>Cu<sub>3</sub>O<sub>6</sub>.

Figure 7 The  $I-V$  and conductivity ( $dI/dV$ ) curves of a cleaved surface of Bi<sub>2</sub>Cu<sub>3</sub>O<sub>6</sub>.

Figure 8 The  $I-V$  and conductivity ( $dI/dV$ ) curves of a cleaved surface of Bi<sub>2</sub>Cu<sub>3</sub>O<sub>6</sub>.

Figure 9 The  $I-V$  and conductivity ( $dI/dV$ ) curves of a cleaved surface of Bi<sub>2</sub>Cu<sub>3</sub>O<sub>6</sub>.

Figure 10 The  $I-V$  and conductivity ( $dI/dV$ ) curves of a cleaved surface of Bi<sub>2</sub>Cu<sub>3</sub>O<sub>6</sub>.

Figure 11 The  $I-V$  and conductivity ( $dI/dV$ ) curves of a cleaved surface of Bi<sub>2</sub>Cu<sub>3</sub>O<sub>6</sub>.

Figure 12 The  $I-V$  and conductivity ( $dI/dV$ ) curves of a cleaved surface of Bi<sub>2</sub>Cu<sub>3</sub>O<sub>6</sub>.

Figure 13 The  $I-V$  and conductivity ( $dI/dV$ ) curves of a cleaved surface of Bi<sub>2</sub>Cu<sub>3</sub>O<sub>6</sub>.

Figure 14 The  $I-V$  and conductivity ( $dI/dV$ ) curves of a cleaved surface of Bi<sub>2</sub>Cu<sub>3</sub>O<sub>6</sub>.

Figure 15 The  $I-V$  and conductivity ( $dI/dV$ ) curves of a cleaved surface of Bi<sub>2</sub>Cu<sub>3</sub>O<sub>6</sub>.

Figure 16 The  $I-V$  and conductivity ( $dI/dV$ ) curves of a cleaved surface of Bi<sub>2</sub>Cu<sub>3</sub>O<sub>6</sub>.

Figure 17 The  $I-V$  and conductivity ( $dI/dV$ ) curves of a cleaved surface of Bi<sub>2</sub>Cu<sub>3</sub>O<sub>6</sub>.

Figure 18 The  $I-V$  and conductivity ( $dI/dV$ ) curves of a cleaved surface of Bi<sub>2</sub>Cu<sub>3</sub>O<sub>6</sub>.

Figure 19 The  $I-V$  and conductivity ( $dI/dV$ ) curves of a cleaved surface of Bi<sub>2</sub>Cu<sub>3</sub>O<sub>6</sub>.

Figure 20 The  $I-V$  and conductivity ( $dI/dV$ ) curves of a cleaved surface of Bi<sub>2</sub>Cu<sub>3</sub>O<sub>6</sub>.

Figure 21 The  $I-V$  and conductivity ( $dI/dV$ ) curves of a cleaved surface of Bi<sub>2</sub>Cu<sub>3</sub>O<sub>6</sub>.

Figure 22 The  $I-V$  and conductivity ( $dI/dV$ ) curves of a cleaved surface of Bi<sub>2</sub>Cu<sub>3</sub>O<sub>6</sub>.

Figure 23 The  $I-V$  and conductivity ( $dI/dV$ ) curves of a cleaved surface of Bi<sub>2</sub>Cu<sub>3</sub>O<sub>6</sub>.

Figure 24 The  $I-V$  and conductivity ( $dI/dV$ ) curves of a cleaved surface of Bi<sub>2</sub>Cu<sub>3</sub>O<sub>6</sub>.

Figure 25 The  $I-V$  and conductivity ( $dI/dV$ ) curves of a cleaved surface of Bi<sub>2</sub>Cu<sub>3</sub>O<sub>6</sub>.

Figure 26 The  $I-V$  and conductivity ( $dI/dV$ ) curves of a cleaved surface of Bi<sub>2</sub>Cu<sub>3</sub>O<sub>6</sub>.

Figure 27 The  $I-V$  and conductivity ( $dI/dV$ ) curves of a cleaved surface of Bi<sub>2</sub>Cu<sub>3</sub>O<sub>6</sub>.

Figure 28 The  $I-V$  and conductivity ( $dI/dV$ ) curves of a cleaved surface of Bi<sub>2</sub>Cu<sub>3</sub>O<sub>6</sub>.

Figure 29 The  $I-V$  and conductivity ( $dI/dV$ ) curves of a cleaved surface of Bi<sub>2</sub>Cu<sub>3</sub>O<sub>6</sub>.

Figure 30 The  $I-V$  and conductivity ( $dI/dV$ ) curves of a cleaved surface of Bi<sub>2</sub>Cu<sub>3</sub>O<sub>6</sub>.

Figure 31 The  $I-V$  and conductivity ( $dI/dV$ ) curves of a cleaved surface of Bi<sub>2</sub>Cu<sub>3</sub>O<sub>6</sub>.

Figure 32 The  $I-V$  and conductivity ( $dI/dV$ ) curves of a cleaved surface of Bi<sub>2</sub>Cu<sub>3</sub>O<sub>6</sub>.

Figure 33 The  $I-V$  and conductivity ( $dI/dV$ ) curves of a cleaved surface of Bi<sub>2</sub>Cu<sub>3</sub>O<sub>6</sub>.

Figure 34 The  $I-V$  and conductivity ( $dI/dV$ ) curves of a cleaved surface of Bi<sub>2</sub>Cu<sub>3</sub>O<sub>6</sub>.

Figure 35 The  $I-V$  and conductivity ( $dI/dV$ ) curves of a cleaved surface of Bi<sub>2</sub>Cu<sub>3</sub>O<sub>6</sub>.

Figure 36 The  $I-V$  and conductivity ( $dI/dV$ ) curves of a cleaved surface of Bi<sub>2</sub>Cu<sub>3</sub>O<sub>6</sub>.

Figure 37 The  $I-V$  and conductivity ( $dI/dV$ ) curves of a cleaved surface of Bi<sub>2</sub>Cu<sub>3</sub>O<sub>6</sub>.

Figure 38 The  $I-V$  and conductivity ( $dI/dV$ ) curves of a cleaved surface of Bi<sub>2</sub>Cu<sub>3</sub>O<sub>6</sub>.

Figure 39 The  $I-V$  and conductivity ( $dI/dV$ ) curves of a cleaved surface of Bi<sub>2</sub>Cu<sub>3</sub>O<sub>6</sub>.

Figure 40 The  $I-V$  and conductivity ( $dI/dV$ ) curves of a cleaved surface of Bi<sub>2</sub>Cu<sub>3</sub>O<sub>6</sub>.

Figure 41 The  $I-V$  and conductivity ( $dI/dV$ ) curves of a cleaved surface of Bi<sub>2</sub>Cu<sub>3</sub>O<sub>6</sub>.

Figure 42 The  $I-V$  and conductivity ( $dI/dV$ ) curves of a cleaved surface of Bi<sub>2</sub>Cu<sub>3</sub>O<sub>6</sub>.

Figure 43 The  $I-V$  and conductivity ( $dI/dV$ ) curves of a cleaved surface of Bi<sub>2</sub>Cu<sub>3</sub>O<sub>6</sub>.

Figure 44 The  $I-V$  and conductivity ( $dI/dV$ ) curves of a cleaved surface of Bi<sub>2</sub>Cu<sub>3</sub>O<sub>6</sub>.

Figure 45 The  $I-V$  and conductivity ( $dI/dV$ ) curves of a cleaved surface of Bi<sub>2</sub>Cu<sub>3</sub>O<sub>6</sub>.

Figure 46 The  $I-V$  and conductivity ( $dI/dV$ ) curves of a cleaved surface of Bi<sub>2</sub>Cu<sub>3</sub>O<sub>6</sub>.

Figure 47 The  $I-V$  and conductivity ( $dI/dV$ ) curves of a cleaved surface of Bi<sub>2</sub>Cu<sub>3</sub>O<sub>6</sub>.

Figure 48 The  $I-V$  and conductivity ( $dI/dV$ ) curves of a cleaved surface of Bi<sub>2</sub>Cu<sub>3</sub>O<sub>6</sub>.

Figure 49 The  $I-V$  and conductivity ( $dI/dV$ ) curves of a cleaved surface of Bi<sub>2</sub>Cu<sub>3</sub>O<sub>6</sub>.

Figure 50 The  $I-V$  and conductivity ( $dI/dV$ ) curves of a cleaved surface of Bi<sub>2</sub>Cu<sub>3</sub>O<sub>6</sub>.

Figure 51 The  $I-V$  and conductivity ( $dI/dV$ ) curves of a cleaved surface of Bi<sub>2</sub>Cu<sub>3</sub>O<sub>6</sub>.

Figure 52 The  $I-V$  and conductivity ( $dI/dV$ ) curves of a cleaved surface of Bi<sub>2</sub>Cu<sub>3</sub>O<sub>6</sub>.

Figure 53 The  $I-V$  and conductivity ( $dI/dV$ ) curves of a cleaved surface of Bi<sub>2</sub>Cu<sub>3</sub>O<sub>6</sub>.

Figure 54 The  $I-V$  and conductivity ( $dI/dV$ ) curves of a cleaved surface of Bi<sub>2</sub>Cu<sub>3</sub>O<sub>6</sub>.

Figure 55 The  $I-V$  and conductivity ( $dI/dV$ ) curves of a cleaved surface of Bi<sub>2</sub>Cu<sub>3</sub>O<sub>6</sub>.

Figure 56 The  $I-V$  and conductivity ( $dI/dV$ ) curves of a cleaved surface of Bi<sub>2</sub>Cu<sub>3</sub>O<sub>6</sub>.

Figure 57 The  $I-V$  and conductivity ( $dI/dV$ ) curves of a cleaved surface of Bi<sub>2</sub>Cu<sub>3</sub>O<sub>6</sub>.

Figure 58 The  $I-V$  and conductivity ( $dI/dV$ ) curves of a cleaved surface of Bi<sub>2</sub>Cu<sub>3</sub>O<sub>6</sub>.

Figure 59 The  $I-V$  and conductivity ( $dI/dV$ ) curves of a cleaved surface of Bi<sub>2</sub>Cu<sub>3</sub>O<sub>6</sub>.

Figure 60 The  $I-V$  and conductivity ( $dI/dV$ ) curves of a cleaved surface of Bi<sub>2</sub>Cu<sub>3</sub>O<sub>6</sub>.

Figure 61 The  $I-V$  and conductivity ( $dI/dV$ ) curves of a cleaved surface of Bi<sub>2</sub>Cu<sub>3</sub>O<sub>6</sub>.

Figure 62 The  $I-V$  and conductivity ( $dI/dV$ ) curves of a cleaved surface of Bi<sub>2</sub>Cu<sub>3</sub>O<sub>6</sub>.

Figure 63 The  $I-V$  and conductivity ( $dI/dV$ ) curves of a cleaved surface of Bi<sub>2</sub>Cu<sub>3</sub>O<sub>6</sub>.

Figure 64 The  $I-V$  and conductivity ( $dI/dV$ ) curves of a cleaved surface of Bi<sub>2</sub>Cu<sub>3</sub>O<sub>6</sub>.

Figure 65 The  $I-V$  and conductivity ( $dI/dV$ ) curves of a cleaved surface of Bi<sub>2</sub>Cu<sub>3</sub>O<sub>6</sub>.

Figure 66 The  $I-V$  and conductivity ( $dI/dV$ ) curves of a cleaved surface of Bi<sub>2</sub>Cu<sub>3</sub>O<sub>6</sub>.

Figure 67 The  $I-V$  and conductivity ( $dI/dV$ ) curves of a cleaved surface of Bi<sub>2</sub>Cu<sub>3</sub>O<sub>6</sub>.

Figure 68 The  $I-V$  and conductivity ( $dI/dV$ ) curves of a cleaved surface of Bi<sub>2</sub>Cu<sub>3</sub>O<sub>6</sub>.

Figure 69 The  $I-V$  and conductivity ( $dI/dV$ ) curves of a cleaved surface of Bi<sub>2</sub>Cu<sub>3</sub>O<sub>6</sub>.

Figure 70 The  $I-V$  and conductivity ( $dI/dV$ ) curves of a cleaved surface of Bi<sub>2</sub>Cu<sub>3</sub>O<sub>6</sub>.

Figure 71 The  $I-V$  and conductivity ( $dI/dV$ ) curves of a cleaved surface of Bi<sub>2</sub>Cu<sub>3</sub>O<sub>6</sub>.

Figure 72 The  $I-V$  and conductivity ( $dI/dV$ ) curves of a cleaved surface of Bi<sub>2</sub>Cu<sub>3</sub>O<sub>6</sub>.

Figure 73 The  $I-V$  and conductivity ( $dI/dV$ ) curves of a cleaved surface of Bi<sub>2</sub>Cu<sub>3</sub>O<sub>6</sub>.

Figure 74 The  $I-V$  and conductivity ( $dI/dV$ ) curves of a cleaved surface of Bi<sub>2</sub>Cu<sub>3</sub>O<sub>6</sub>.

Figure 75 The  $I-V$  and conductivity ( $dI/dV$ ) curves of a cleaved surface of Bi<sub>2</sub>Cu<sub>3</sub>O<sub>6</sub>.

Figure 76 The  $I-V$  and conductivity ( $dI/dV$ ) curves of a cleaved surface of Bi<sub>2</sub>Cu<sub>3</sub>O<sub>6</sub>.

Figure 77 The  $I-V$  and conductivity ( $dI/dV$ ) curves of a cleaved surface of Bi<sub>2</sub>Cu<sub>3</sub>O<sub>6</sub>.

Figure 78 The  $I-V$  and conductivity ( $dI/dV$ ) curves of a cleaved surface of Bi<sub>2</sub>Cu<sub>3</sub>O<sub>6</sub>.

Figure 79 The  $I-V$  and conductivity ( $dI/dV$ ) curves of a cleaved surface of Bi<sub>2</sub>Cu<sub>3</sub>O<sub>6</sub>.

Figure 80 The  $I-V$  and conductivity ( $dI/dV$ ) curves of a cleaved surface of Bi<sub>2</sub>Cu<sub>3</sub>O<sub>6</sub>.

Figure 81 The  $I-V$  and conductivity ( $dI/dV$ ) curves of a cleaved surface of Bi<sub>2</sub>Cu<sub>3</sub>O<sub>6</sub>.

Figure 82 The  $I-V$  and conductivity ( $dI/dV$ ) curves of a cleaved surface of Bi<sub>2</sub>Cu<sub>3</sub>O<sub>6</sub>.

Figure 83 The  $I-V$  and conductivity ( $dI/dV$ ) curves of a cleaved surface of Bi<sub>2</sub>Cu<sub>3</sub>O<sub>6</sub>.

Figure 84 The  $I-V$  and conductivity ( $dI/dV$ ) curves of a cleaved surface of Bi<sub>2</sub>Cu<sub>3</sub>O<sub>6</sub>.

Figure 85 The  $I-V$  and conductivity ( $dI/dV$ ) curves of a cleaved surface of Bi<sub>2</sub>Cu<sub>3</sub>O<sub>6</sub>.

Figure 86 The  $I-V$  and conductivity ( $dI/dV$ ) curves of a cleaved surface of Bi<sub>2</sub>Cu<sub>3</sub>O<sub>6</sub>.

Figure 87 The  $I-V$  and conductivity ( $dI/dV$ ) curves of a cleaved surface of Bi<sub>2</sub>Cu<sub>3</sub>O<sub>6</sub>.

Figure 88 The  $I-V$  and conductivity ( $dI/dV$ ) curves of a cleaved surface of Bi<sub>2</sub>Cu<sub>3</sub>O<sub>6</sub>.

Figure 89 The  $I-V$  and conductivity ( $dI/dV$ ) curves of a cleaved surface of Bi<sub>2</sub>Cu<sub>3</sub>O<sub>6</sub>.

Figure 90 The  $I-V$  and conductivity ( $dI/dV$ ) curves of a cleaved surface of Bi<sub>2</sub>Cu<sub>3</sub>O<sub>6</sub>.

Figure 91 The  $I-V$  and conductivity ( $dI/dV$ ) curves of a cleaved surface of Bi<sub>2</sub>Cu<sub>3</sub>O<sub>6</sub>.

Figure 92 The  $I-V$  and conductivity ( $dI/dV$ ) curves of a cleaved surface of Bi<sub>2</sub>Cu<sub>3</sub>O<sub>6</sub>.

Figure 93 The  $I-V$  and conductivity ( $dI/dV$ ) curves of a cleaved surface of Bi<sub>2</sub>Cu<sub>3</sub>O<sub>6</sub>.

Figure 94 The  $I-V$  and conductivity ( $dI/dV$ ) curves of a cleaved surface of Bi<sub>2</sub>Cu<sub>3</sub>O<sub>6</sub>.

Figure 95 The  $I-V$  and conductivity ( $dI/dV$ ) curves of a cleaved surface of Bi<sub>2</sub>Cu<sub>3</sub>O<sub>6</sub>.

Figure 96 The  $I-V$  and conductivity ( $dI/dV$ ) curves of a cleaved surface of Bi<sub>2</sub>Cu<sub>3</sub>O<sub>6</sub>.

Figure 97 The  $I-V$  and conductivity ( $dI/dV$ ) curves of a cleaved surface of Bi<sub>2</sub>Cu<sub>3</sub>O<sub>6</sub>.

Figure 98 The  $I-V$  and conductivity ( $dI/dV$ ) curves of a cleaved surface of Bi<sub>2</sub>Cu<sub>3</sub>O<sub>6</sub>.

Figure 99 The  $I-V$  and conductivity ( $dI/dV$ ) curves of a cleaved surface of Bi<sub>2</sub>Cu<sub>3</sub>O<sub>6</sub>.

Figure 100 The  $I-V$  and conductivity ( $dI/dV$ ) curves of a cleaved surface of Bi<sub>2</sub>Cu<sub>3</sub>O<sub>6</sub>.

Figure 101 The  $I-V$  and conductivity ( $dI/dV$ ) curves of a cleaved surface of Bi<sub>2</sub>Cu<sub>3</sub>O<sub>6</sub>.

Figure 102 The  $I-V$  and conductivity ( $dI/dV$ ) curves of a cleaved surface of Bi<sub>2</sub>Cu<sub>3</sub>O<sub>6</sub>.

Figure 103 The  $I-V$  and conductivity ( $dI/dV$ ) curves of a cleaved surface of Bi<sub>2</sub>Cu<sub>3</sub>O<sub>6</sub>.

Figure 104 The  $I-V$  and conductivity ( $dI/dV$ ) curves of a cleaved surface of Bi<sub>2</sub>Cu<sub>3</sub>O<sub>6</sub>.

Figure 105 The  $I-V$  and conductivity ( $dI/dV$ ) curves of a cleaved surface of Bi<sub>2</sub>Cu<sub>3</sub>O<sub>6</sub>.

Figure 106 The  $I-V$  and conductivity ( $dI/dV$ ) curves of a cleaved surface of Bi<sub>2</sub>Cu<sub>3</sub>O<sub>6</sub>.

Figure 107 The  $I-V$  and conductivity ( $dI/dV$ ) curves of a cleaved surface of Bi<sub>2</sub>Cu<sub>3</sub>O<sub>6</sub>.

Figure 108 The  $I-V$  and conductivity ( $dI/dV$ ) curves of a cleaved surface of Bi<sub>2</sub>Cu<sub>3</sub>O<sub>6</sub>.

Figure 109 The  $I-V$  and conductivity ( $dI/dV$ ) curves of a cleaved surface of Bi<sub>2</sub>Cu<sub>3</sub>O<sub>6</sub>.

Figure



# 科研论文配图的建议

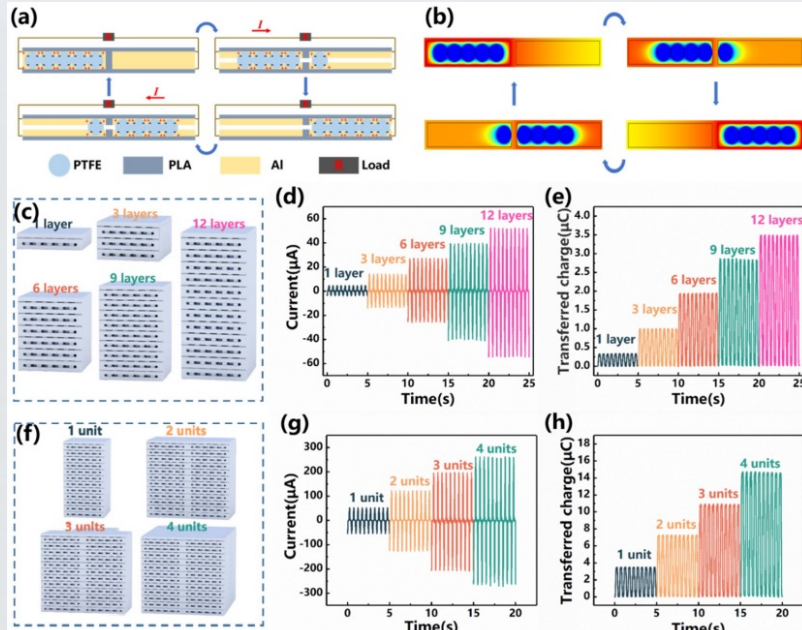
论文——用数据说话，用图片表达，用逻辑自洽

➤ 图片是写作中最重要的一环，要求既包含数据，又必须体现论文的逻辑关系

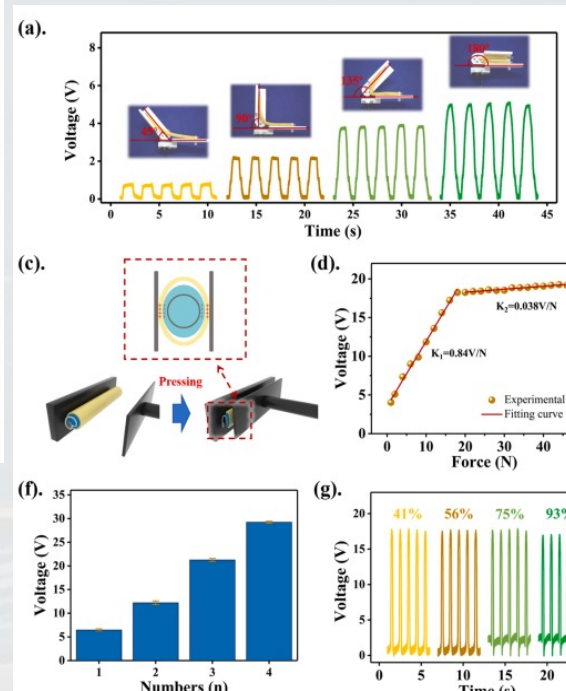
Tips

1. 配色要以突出关键数据、展示逻辑关系为**首要原则**。
2. 尽量选**柔和**的颜色，避免过明、过暗、过亮冷色调。
- 3. 一篇论文的配图，选取一个**主色调**（ $1/3$ 到一半）、使用**近似色**作为辅助色。其他颜色为**互补色、组合色**。

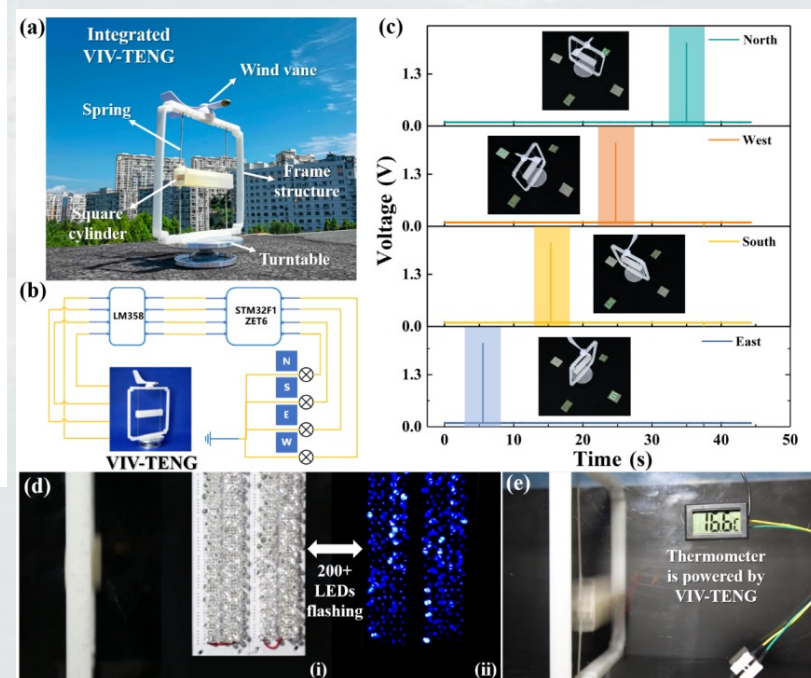
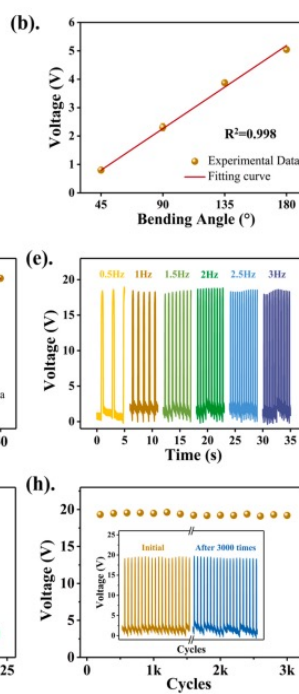
配色要以突出关键数据、展示逻辑关系为首要原则，同时尽可能采取示意图数据图相组合的形式



Hao Wang et al., *Nanomaterials*, 2022



Cong Zhao et al., *Nano energy*, 2022



Yan Wang et al., *Nano research*, 2021

# 一篇论文的配图，选取一个主色调（1/3到一半）、使用近似色作为辅助色。其他颜色为互补色、组合色

Research

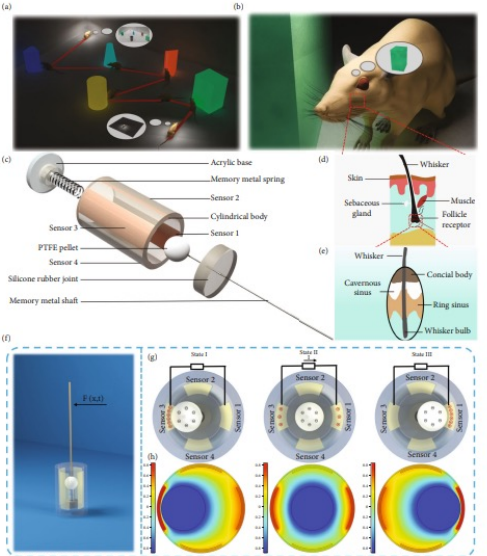


FIGURE 1: Structure and working mechanism of a TWS. (a) A mouse in darkness explores the environment with its whiskers. (b) Measuring both the orientations and distances from obstacles. (c) Location of tactile receptors beneath the surface of the skin. (d) The structure and innervation of a rat whisker follicle. (e) Basic structure of the bionic follicle sensor. (f) Frontal view of the working components. (g) Schematic charge distribution as the PTFE pellet moves. (h) Simulation results showing the potential distribution between the PTFE pellet and Cu film.

and then reaches a plateau. This is because increasing the displacement  $w_x$  can decrease the distance between the PTFE pellet and Cu electrode and increase their contact forces. From [22], increasing mechanical compression between the PTFE pellet and Cu electrode causes an increased output voltage. However, due to material limita-

tions and the size of the TWS, the output voltage saturates the sensor. Moreover, a leave-one-out cross-validation (LOOCV) strategy was used to test the model, and the detection accuracy and generalization performance of these models are shown in Figure 2(c). This confirms that the quadratic model has a high correlation coefficient of

3

4

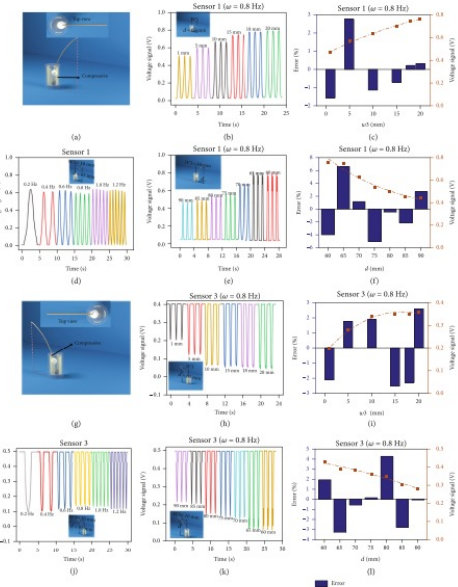


FIGURE 2: Experimental results. (a) The 3DMax model of the whisker sensor and its deflection along the 1 direction. (b) Response due to bending by  $w_x = 1 \text{ mm} - 20 \text{ mm}$  in the 1 direction. (c) LOOCV validation for evaluating accuracy and generalization performance of 1 regarding  $w_x$ . (d) Response from 0.2 Hz to 1.2 Hz in the 1 direction. (e) Response to bending  $d = 60 \text{ mm} - 90 \text{ mm}$  along the 3 direction. (f) LOOCV validation for evaluating accuracy and generalization performance of 1 regarding  $d$ . (g) 3DMax model of a whisker and deformation along the 3 direction from its relaxed state. (h) Response due to bending by  $w_y = 1 \text{ mm} - 20 \text{ mm}$  along the 3 direction. (i) LOOCV validation for evaluating accuracy and generalization performance of 3 regarding  $w_y$ . (j) Response performance at height  $d = 60 \text{ mm} - 90 \text{ mm}$  in the 3 direction. (k) LOOCV validation for evaluating accuracy and generalization performance of 3 regarding  $d$ .

Research

6

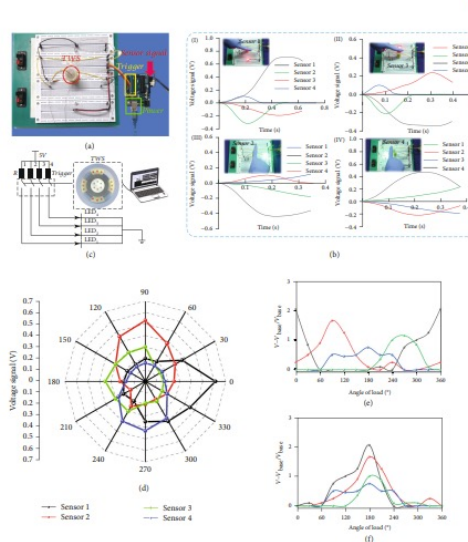


FIGURE 3: Experimental results. (a) Experimental electronic setup. (b) Demonstration of TWS as a sensitive load switch control and its corresponding output voltage signal. (c) Electronic module used for potential application demonstrations, such as controlling LED lights. (d) Directional patterns of the TWS. (e) Rotation from  $0^\circ$  to  $360^\circ$  and  $\Delta V$  for each angle with the same load applied. (f) The results of (e) were replotted with  $\theta$  defined.

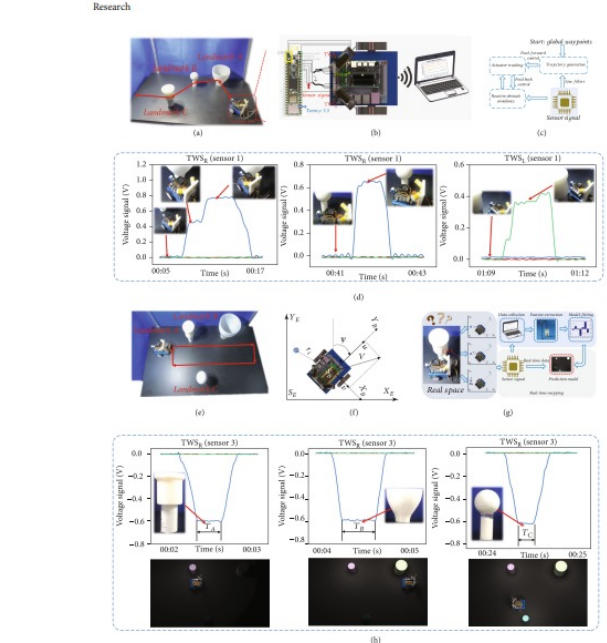
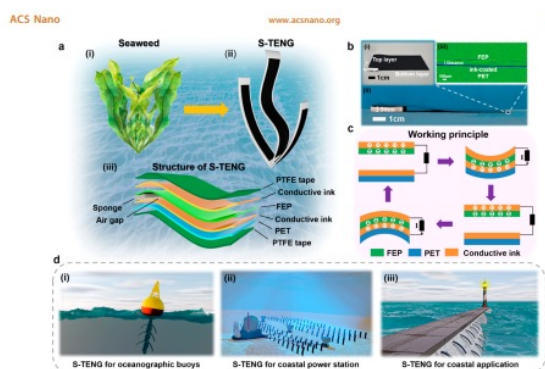
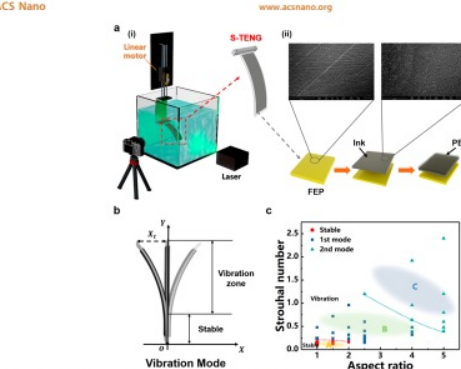


FIGURE 4: Experimental results. (a) Photographs of the actual workspace for reactive obstacle avoidance. (b) Electronic module used for potential application demonstrations, such as reactive obstacle avoidance. (c) Overview of the closed-loop control system for reactive obstacle avoidance. (d) Voltage signal measured at landmarks A, B, and C. (e) Photographs of the actual workspace used for local mapping. (f) Reference frames BODY reference frame and ND reference frame. (g) Local mapping process, where sensory information is applied for model fitting and real-time model prediction. (h) Voltage signal measured at landmarks A, B, and C.

# 一篇论文的配图，选取一个主色调（1/3到一半）、使用近似色作为辅助色。其他颜色为互补色、组合色



**Figure 1.** Schematic drawing of the S-TENG and its applications: (a, i) seaweed, the biotic prototype of the S-TENG; (a, ii) the S-TENG surface morphology on the S-TENG; (c) Working mechanism of the S-TENG. (d) Applications of the S-TENG on the marine internet of things.



**Figure 2.** Experimental apparatus and vibration characteristics of the S-TENG. (a, i) Experimental apparatus of the S-TENG; (a, ii) scanning electron microscope (SEM) photo of the FEP and conductive ink-coated PET; (b) 1st mode of the S-TENG and coordinate system selection diagram; (c) the vibration regime map of the S-TENG.

random wave induced motions. The T-TENG appears to be a quite effective approach of large scale wave energy harvesting. An *et al.*<sup>1</sup> have created a working scaled TENG (WF-TENG) wave energy converter. Vibration of ocean waves with respect to the wave parameters and the structural parameters were investigated systematically. A maximum peak of 6.5 mW and an average power of 0.28 mW were obtained by the WF-TENG, which is capable of powering a digital thermometer. In a study on a fully enclosed TENG wave energy converter published by Wang *et al.*,<sup>2</sup> optimizations of materials and structures were conducted. Low frequency wave energy was converted to power light-emitting diodes (LEDs) and to different sensors connected to the Internet of Things (IoT). In general, those published TENGs have exhibited advantages such as having a simple structure and low cost and being lightweight and robust. However, most of the previously published wave energy TENGs are designed for harvesting energy from the ocean surface waves. Though the majority of the marine applications are surface ones, supplying renewable electricity to underwater applications should not be left out. In order to encompass energy harvesters in a larger volume of the ocean to provide power to the IoT sensors, a wave energy TENG that can work at both surface areas (float) and underwater areas (submerged) is desperately needed. On top of that, the wave energy TENG will be more impressive if it can be easily integrated with the marine equipment.

In this study, a flexible seaweed-like triboelectric nanogenerator (S-TENG) is first proposed to supply *in situ* power to marine distributed sensors. The idea of developing a seaweed-like TENG is inspired because of the close observations we made on a common sea plant, seaweed. The process in which the seaweed vibrates with the wave is measured by the electron microscope LEXT OLS4000, which is shown in Figure 1b(ii). From the above, the air gap due to the sponge and surface morphology of the FEP and ink-coated PET film can be observed. The device (Figure S1) with concave structures makes contact electrification and electrostatic induction simultaneously, ensuring a good correspondence between the wave and electrical signal of the S-TENG. It is better to set the two triboelectric layers to "contact" state initially so that the TENG could produce output even with the wave. When the wave passes through the S-TENG, two triboelectric layers are brought into contact with each other, and the contact area correlates with the wave excitation.

As the S-TENG vibrates periodically under the wave excitations, the FEP membrane will make contact with and separate from the PET membrane periodically as shown in Figure 1a(i). After certain contacts with the ink-coated PET, the FEP membrane will become negatively charged. According to the essence of electrostatic induction, an equivalent amount of positive charge will occupy the ink electrode on the PET when the ink electrodes of PET and the FEP membrane have sufficient contact. As the S-TENG bends, the electrons will flow from the electrode attached to the FEP to the electrode attached to the PET (through the external circuit); therefore, a transient current is generated. Subsequently, as the FEP and ink electrode get separated, the positive charges will flow back to the upper electrode. Due to its high Young's modulus as well as good ink adhesion, the PET and FEP membranes are selected for the other triboelectric friction layers for the S-TENG. The microstructure of the FEP and ink-coated PET film can be observed by a scanning electron

microscope Phenom Pro image as shown in Figure 2a(ii). The device with two wave structures made contact electrification and electrostatic induction simultaneously, ensuring a good correspondence between the wave and electrical signal of the S-TENG.

Certain nondimensional parameters have been applied to represent elasticity and fluid pressure on the structure. The length ( $L$ ) is usually expressed by the nondimensional aspect ratio  $l/w$ ,<sup>10</sup> where  $w$  is the width of the S-TENG. The vibration frequency ( $f$ ) is usually expressed by the Strouhal number ( $S = f/L/U$ ).

The S-TENG's vibration under the wave excitation is a typical forced vibration. The S-TENG can be approximated as a two-dimensional structure with high extensional rigidity and low bending rigidity, which satisfies the Euler-Bernoulli beam equation

$$m\ddot{y}'' + D\dot{y}'\omega^2 - \Delta P = 0 \quad (1)$$

where  $Q$  is the total transferred charge;  $d_0$ ,  $r_0$  and  $S$  represent the thickness of the membrane, the dielectric constant in vacuum, and the area size of the electrode, respectively;  $y$  denotes the displacement between the dielectric membrane and the electrode;  $\sigma$  denotes the charge density. According to the eq 1, the maximum displacement between the dielectric membrane and the electrode determines the maximum output of the S-TENG. The displacement between the dielectric membrane and the electrode changes as the S-TENG vibrates with the wave.

To show the working principle of the S-TENG, the potential distributions across the two electrodes have been analyzed with COMSOL, a finite-element software for Multiphysics analysis as shown in Figure S3. The contour clearly depicts the potential difference driving the current between the two electrodes. Due to its flexible essence, the S-TENG can be applied (as a power supply module) to many marine applications, such as floating buoys (surface), coastal power stations (underwater), and breakwaters (shoreside), as shown in Figure 1d.

**Vibration and Electric Performance of the S-TENG.** As shown in Figure 2a(i), a linear motor was used to simulate the vibration of the S-TENG. The laser and the video imaging was adopted to better observe the vibration performance of the S-TENG. The microstructure of the FEP and ink-coated PET film can be observed by a scanning electron

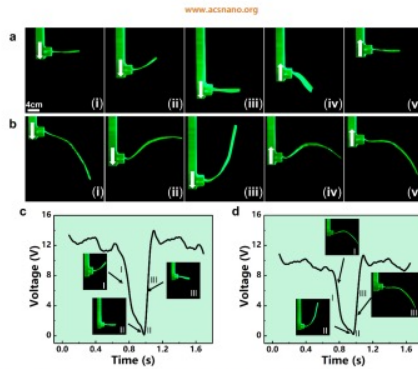


**Figure 3.** Sequential images of vibration behavior and analysis of the electrical signal for the 1st mode. (a) 1st mode: vibration behavior of the S-TENG with the dimensions  $40 \times 80$  mm; (b) 2nd mode: vibration behavior of the S-TENG with the dimensions  $40 \times 200$  mm. The voltage signal of the S-TENG corresponding to (c) the 1st mode; (d) the 2nd mode.

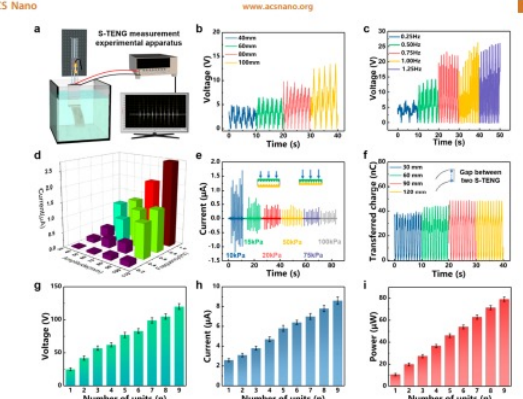


**Figure 4.** Output performance of the S-TENG. (a) Experimental apparatus of the S-TENG. (b) Effect of the frequency of the linear motor's motion on the open-circuit voltage of the S-TENG. (c) the effect of the frequency of the linear motor on the open-circuit voltage of the S-TENG; (d) 3D graph of the output current under different amplitudes and frequencies of the linear motor; (e) the output current of the S-TENGs with different numbers of units; (f) the transferred charge of the S-TENG with different parallel distances; (g) the output voltage of the S-TENGs with different numbers of units; (h) the output current of the S-TENGs with different numbers of units; (i) the output power of the S-TENGs with different numbers of units.

number. The dimension will influence the vibration mode but not the vibration frequency. It is likely that the triboelectric electrons generated by the two opposite cracks cancel out each other, which reduces the electric output of the S-TENG. Therefore, the first mode S-TENG turns out to be better for energy conversion.

As our studies have shown that the  $40 \times 80$  mm S-TENG can be excited to the first mode under a wide range of Strouhal numbers (as Figure 2c), experiments on the S-TENG's electric performance were carried out on the  $40 \times 80$  mm S-TENG. The S-TENG also has X-shaped internal dielectric layers and hydrostatic pressure difference, which is induced by the waves across the structure. Among these parameters, the nondimensional bending stiffness ( $D$ ) is what governs the vibration of a thin two-dimensional structure (e.g., the S-TENG).<sup>5,11,12</sup>  $D$  is defined as

$$D = \frac{Eh^3}{12(1-\nu^2)\rho_i U^2 L^2} \quad (2)$$

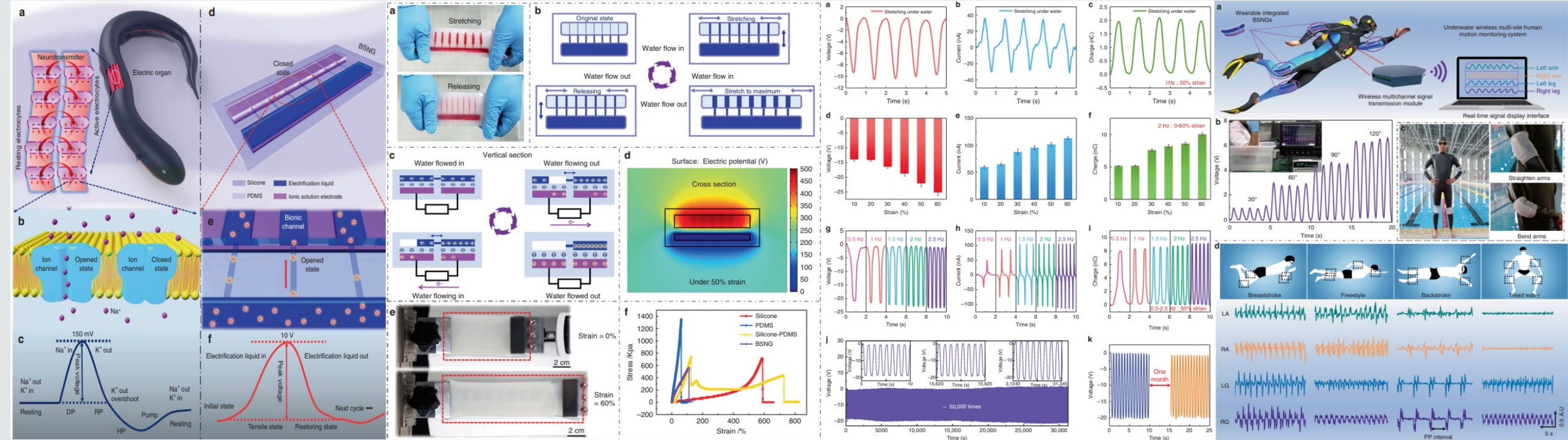
where  $\nu$  is the Poisson's ratio,  $\rho_i$  is the fluid density,  $U$  is the wave velocity,  $h$  is the thickness of the S-TENG,  $L$  is the structure length, and  $E$  is the Young's modulus. Since the

number. The dimension will influence the vibration mode but not the vibration frequency. Figure 2c presents the sequential image of the first mode of the S-TENG, considering that the fluctuated ethylene propylene (FEP) has a relatively low Young's modulus and high electromechanical coupling coefficient, it was selected as the dielectric material in the S-TENG.<sup>5,12</sup> The corresponding material parameters are listed in Table S1. Equations 2 and 3 are the governing equations that determine the coupled fluid and structural motion of the S-TENG depicted in Figure 2b.

One key parameter to evaluate the second order oscillation is the Strouhal number. In the experiments, the Strouhal number was increased from 0.08 to 2.4. The physical dimensions for the experimental samples are listed in Table S2. Figure 2c is the two-dimensional map characterizing the vibration status with respect to the dimensionless parameters. The Strouhal number stays stable when the Strouhal number is within 0.18, and the aspect ratio ranged from 1 to 2. As the Strouhal number and the aspect ratio increased, the S-TENG exhibited the first mode characteristic of a cantilever beam,<sup>5</sup> as shown in Figure 2b. The vibration amplitude of the lower part was nearly zero, while the upper part was the vibration zone with the vibration amplitude increasing toward the trailing edge. As the Strouhal number and the aspect ratio increased further, the vibration gradually transitioned from the first mode (region A) to the second mode (region B). The transition between the first mode and second mode appeared when the Strouhal number ranged from 0.4 to 1.2 and the aspect ratio ranged from 2.5 to 5, as shown in Figure 2c. The S-TENG's vibration is excited by the wave. Theoretically, the vibration frequency equals the wave frequency. According to the experimental results in Figure 2c, when the aspect ratio is constant, the vibration mode is determined by the Strouhal

一篇论文的配图，选取一个主色调（1/3到一半）、使用近似色作为辅助色。其他颜色为互补色、组合色

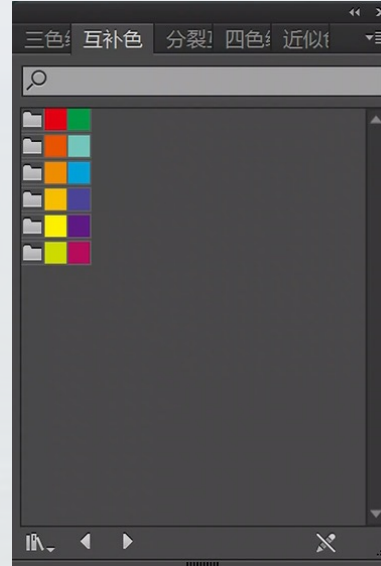
首尾呼应！



Zhou Li et al., *Nature communication*, 2019

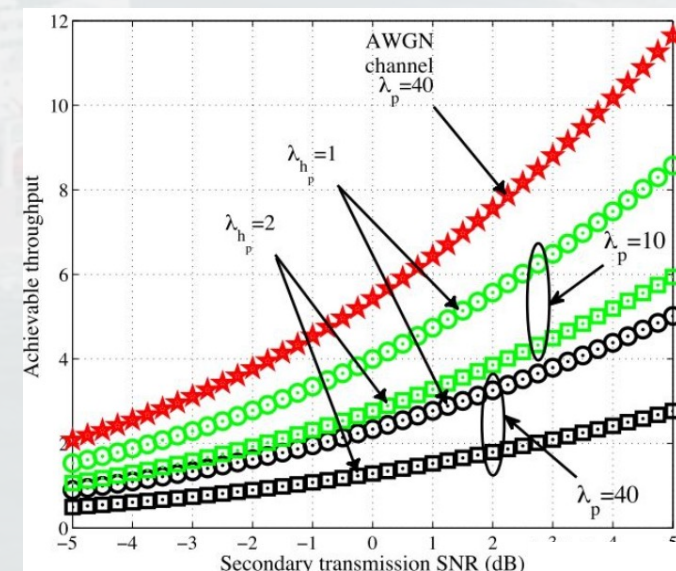
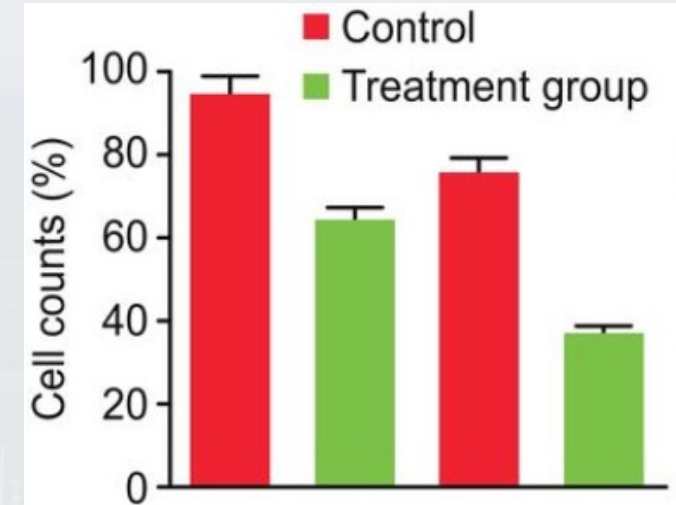


# 近似色、互补色、组合色



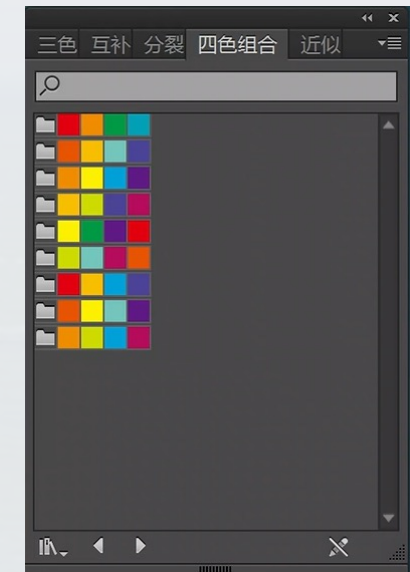
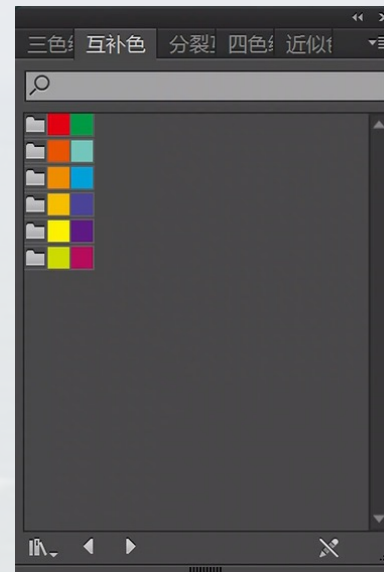
## Tips

1. 两类数据之间最好不要使用互补色，三类及以上可以
2. 尽量选**柔和**的色调，避免饱和度过高/低
3. 颜色不宜过多、过杂，**避免**同一幅图中同时出现红绿色
4. 渐变背景较难驾驭，尽量用近似色



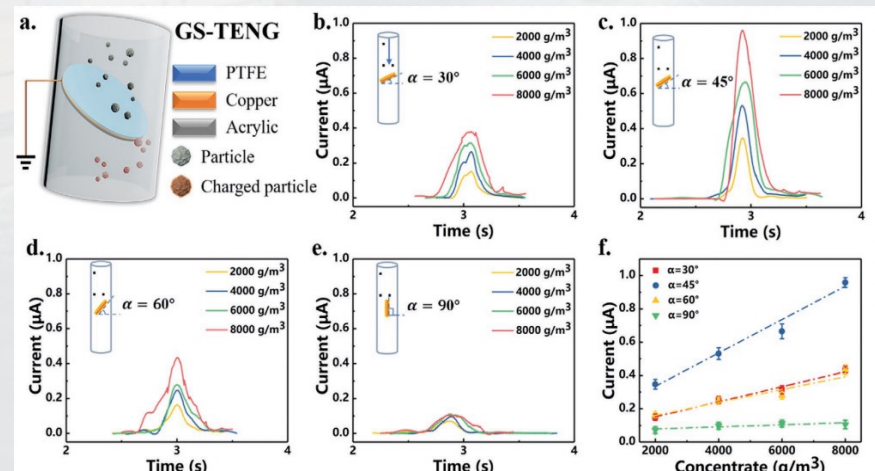
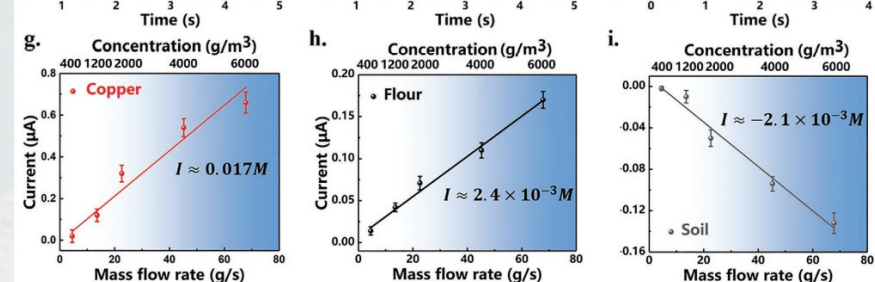
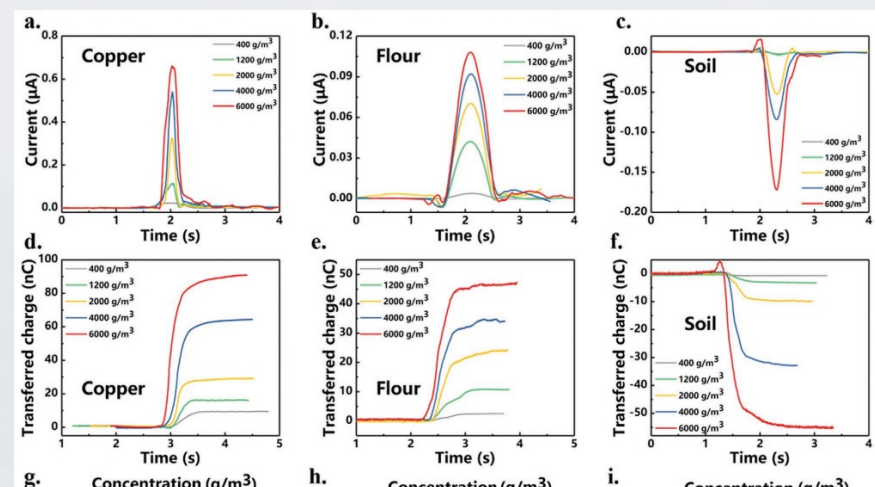


# 近似色、互补色、组合色



## Tips

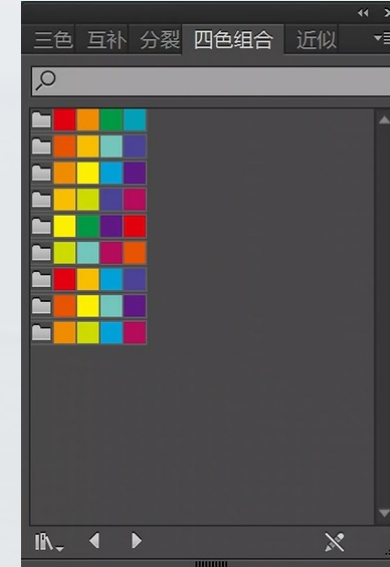
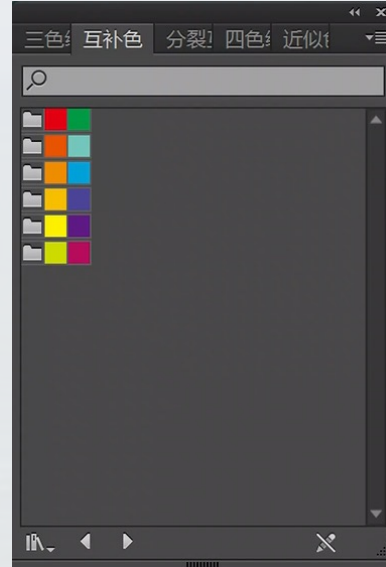
- 两类数据之间最好不要使用红绿互补色，三类及以上可以
- 尽量选柔和的色调，避免饱和度过高/低
- 颜色不宜过多、过杂
- 渐变背景较难驾驭，尽量用近似色



Yan Wang et al., *Adv. Mater. Technol.*, 2021

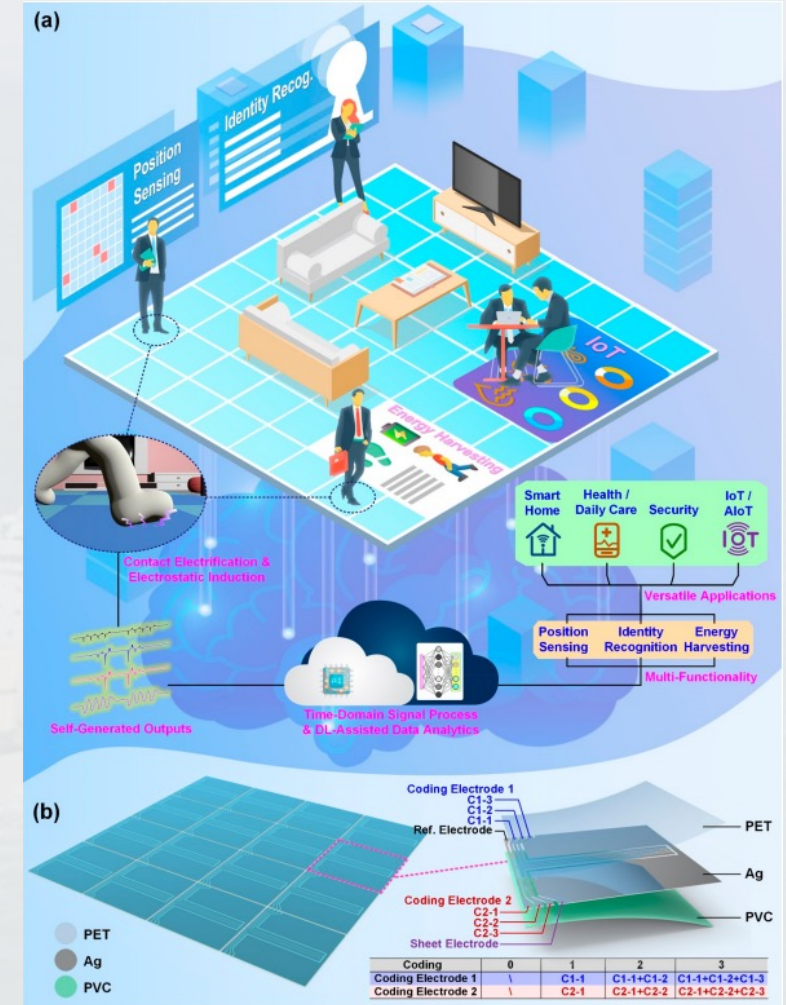


# 近似色、互补色、组合色



## Tips

1. 两类数据之间最好不要使用互补色，三类及以上可以
2. 尽量选**柔和**的色调，避免饱和度过高/低
3. 颜色不宜过多、过杂，**避免**同一幅图中同时出现红绿色
4. 渐变背景较难驾驭，尽量用近似色



Chengkuo Lee et al., ACS nano, 2021



# 常用的配色网站

Color Hunt Palettes > New

Today: #335D2D (8 hearts)

Yesterday: #335D2D (203 hearts)

2 days: #335D2D (276 hearts)

<https://colorhunt.co/>

001 Warm Flame

#ff9a9e → #fad0c4

Copy CSS

002 Night Fade

#a18cd1 → #fbcc2eb

Copy CSS

<https://webgradients.com/>

Cool Blues, Moonlit Asteroid

Cool Sky, Memariani

Anur Lane, Metropolis

By Design, Smokey Dog

<https://uigradients.com/>

CHINESE COLORS

JIANSHILAN (涧石蓝)

C: 73, M: 17, Y: 20, K: 1, R: 102, G: 169, B: 201

Color wheel and names:

- 古鼎灰 (Gǔdǐng huī) #362B2F
- 丁香淡紫 (Dīngxiāng dàn zǐ) #E8D7DF
- 梅红 (Méihóng) #D8357D
- 暗红 (Ànhóng) #D8357D
- 玫瑰红 (Lèiqí hóng) #C95891
- 紫灰 (Zǐhuī) #A8D4E4
- 龙睛鱼紫 (Lóngjīng yúzǐ) #4E2A40
- 青花瓷紫 (Qīnghuācí zǐ) #B0C4DE
- 莲瓣紫 (Liánbàn zǐ) #4E2A40
- 碧玉紫 (Bìyù zǐ) #5D3F51
- 长颈鹿紫 (Chángjǐnglù zǐ) #4E2A40
- 珊瑚紫 (Shāncónghuī) #8B1E4A
- 珊瑚红 (Shāncónghóng) #C95891
- 丹朱红 (Dānzhū hóng) #D8357D
- 丹朱黄 (Dānzhū huáng) #D9A9D9
- 丹朱紫 (Dānzhū zǐ) #C95891
- 丹朱白 (Dānzhū bái) #F0F0F0

<http://zhongguose.com/>



# 论文大图的构思与排版

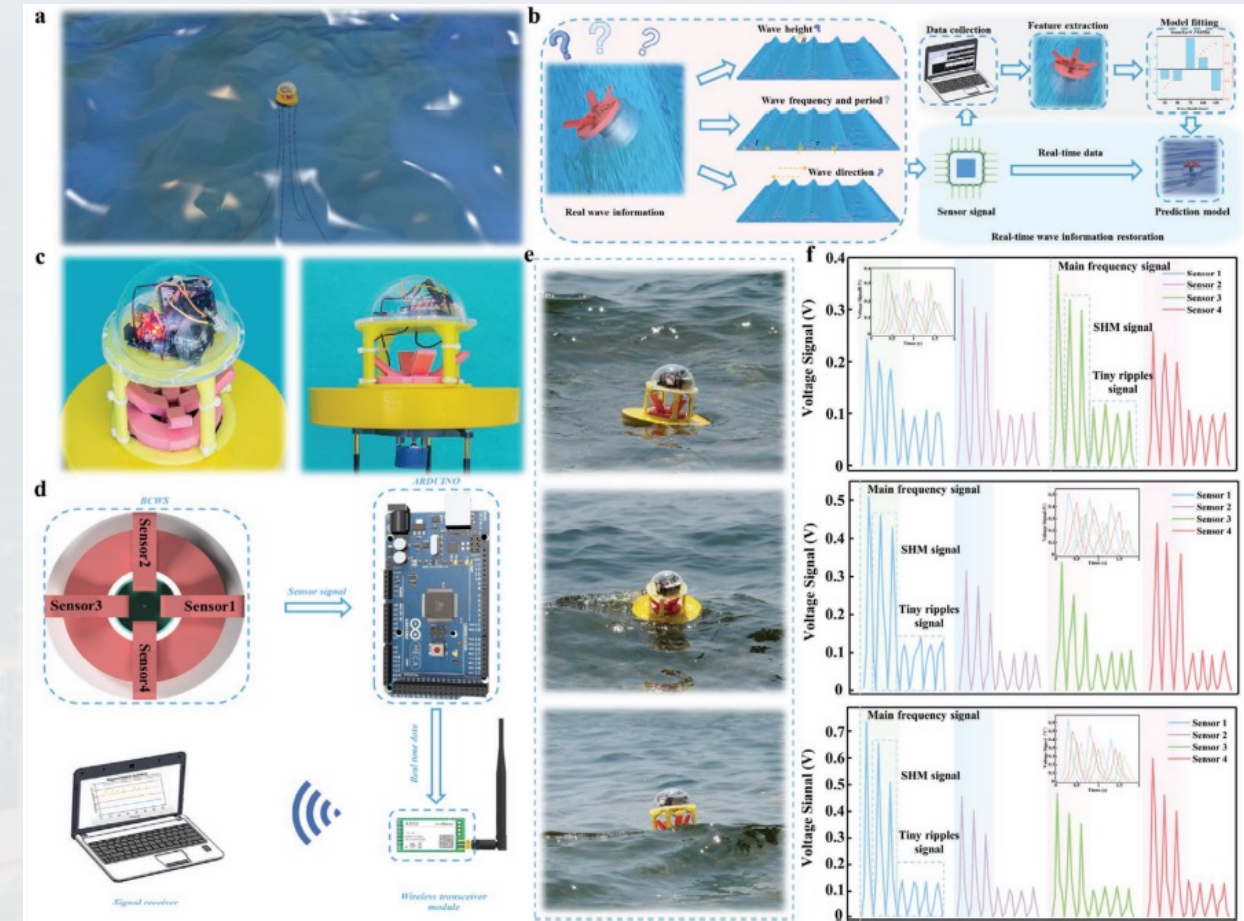
## 1. 正文部分整体框架 ( 5-6张大图 )

- 场景、器件 ( 1-2张 )
- 实验部分 ( 2-4张 )
- 实验演示 ( 1张 )
- 每部分之间逻辑递进

## 2. 每一部分格局框架

- 美化排版 (  $3 \times 2 / 2 \times 2$  )
- 实验部分不建议做 $2 \times 3$
- 每张小图不一定等大 ( 虚线框架 )
- 错落有致、分布均匀
- 多余的数据放Supporting Information

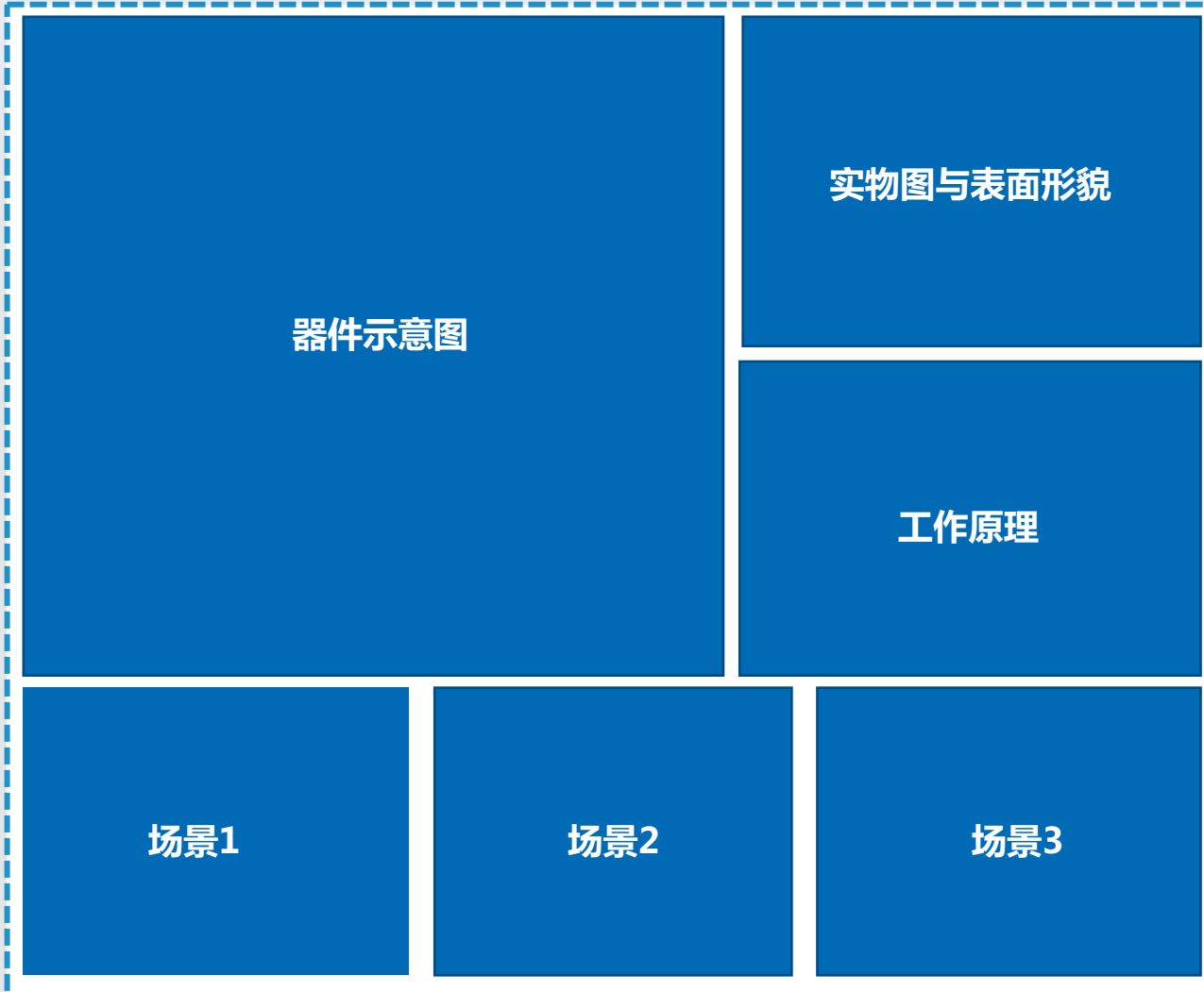
先定框架再下笔 !



Xinyu Wang et al., *Adv. Mater. Technol.*, 2021



# 论文大图的构思与排版



## Tips

1. 背景全白 (RGB255) / 透明
2. 不一定构建外部框架
3. 图片等大、对齐
4. 图片文字批注不用艺术字、不斜体
5. 先定框架，再做细节处理
6. 图片去白对齐、柔化边缘、亮度锐化
7. 用数据图填满大图，而不是用示意  
图填满大图！



# 论文大图的构思与排版



一张六宫格实验数据图的文章工作量远远不够！

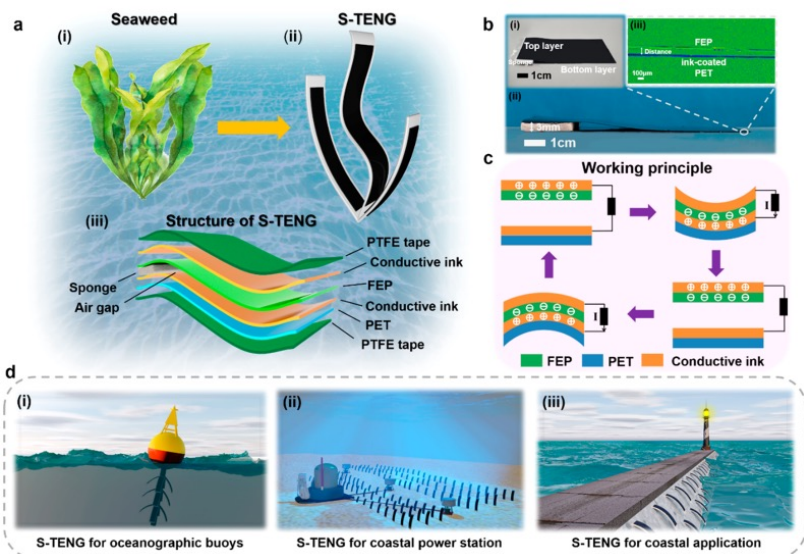
论文的本质依然是用数据说话！

## Tips

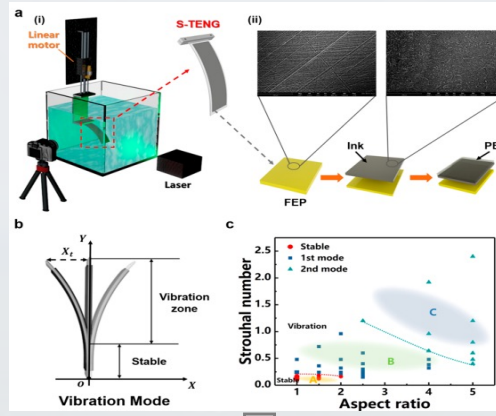
1. 背景全白 ( RGB255 ) / 透明
2. 不一定构建外部框架
3. 图片等大、对齐
4. 图片文字批注不用艺术字、不斜体
5. 先定框架，再做细节处理
6. 图片去白对齐、柔化边缘、亮度锐化
7. 用数据图填满大图，而不是用示意  
图填满大图！
8. 择优择重点，多余的图放SI



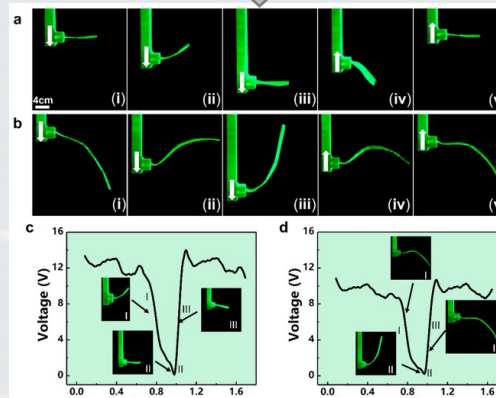
# 总一分一总



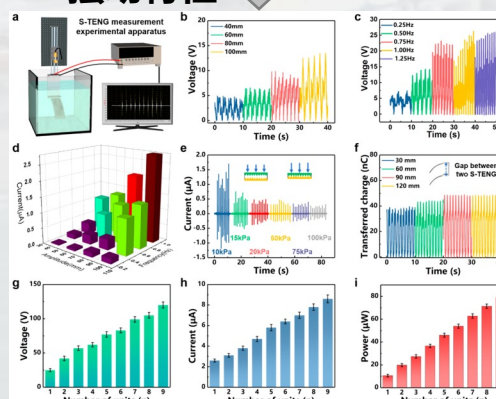
总：× × 场景提出 × × 器件



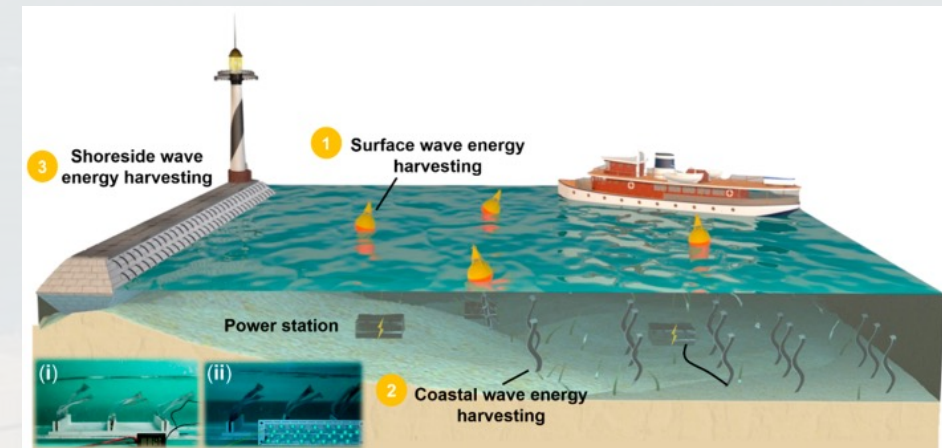
动力学模型 ↓ 实验装置



摆动特性 ↓



最优解 (是什么, 怎么样)



总：× × 器件未来应用于 × × 场景



「01」 论文图片绘制

「02」 汇报PPT绘制

「03」 总结与心得



# 文献汇报PPT的构思与排版

## 1. 逻辑梳理

- 摘要（为什么做、怎么做、结论与展望）
- 研究背景（1页）、实验部分（3-6页）、结论（1页）
- 每部分体现逻辑递进

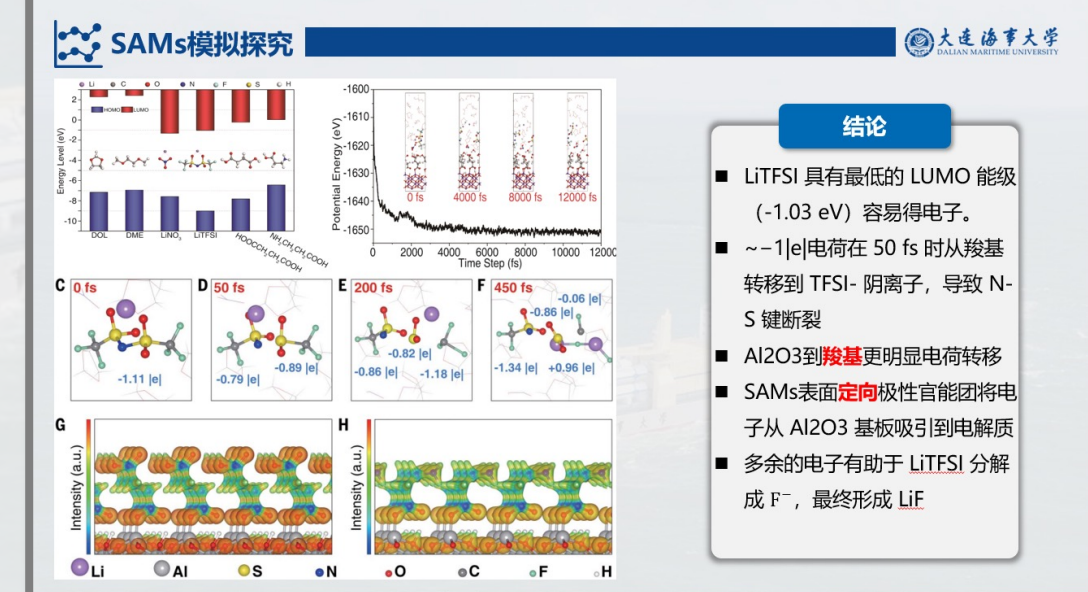
## 2. 每一部分排版

- 研究背景采用递进式
- 主体部分采用图片+结论（左右式、上下式）
- 图文并茂，不等于所有图文复制粘贴！
- 关键字/词/句的提炼与标注

汇报过程又快又准

让别人看懂，让自己说透

体现汇报人自己的思考





# 工作汇报PPT的构思与排版

## 1. 逻辑梳理

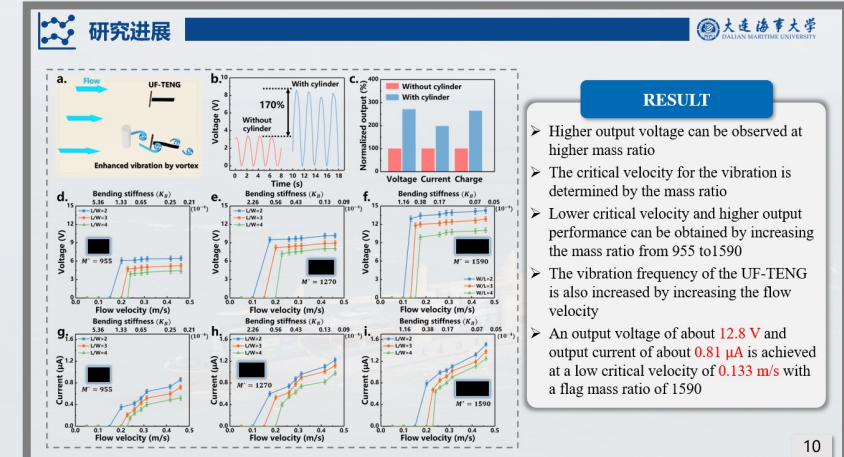
- 研究背景、工作进展、下一步计划
- 合适的应用场景—国内外现状—TENG
- TENG只是一项技术，并非一件产品！

## 2. 排版方式

- 研究背景（1-2页）、**实验进展**（3-6页）结论（1页）
- 图文并茂、关键字/词/句的**提炼与标注**
- “主线任务”（多页）与“支线任务”（1页）进行排版
- 按照时间线定期排列、按进度表定期总结（1页）

**重视迭代过程，保存平时的后处理照片/数据图**

**多拍照，无意的照片可能会是整项工作的点睛之笔！**





「01」学术论文图片绘制

「02」工作汇报PPT绘制

「03」总结与心得



# 总结与心得

技巧很重要，但**逻辑思维**更重要

- 审美需建立在整体性分析上
- 作图/PPT过程体现逻辑
- 保持美观、易懂、趣味性与科学性

## Tips

1. 对整体的把控多思考。
  2. 对细节的处理多练习。
  3. 多参加学术讲座提升自己大局观和思维能力
- 勤能补拙，多学习、多动手锻炼自己。



# 常用科研软件

## 1. 三维模型建立/绘制

- Solidworks
- CAD

## 2. 模型渲染

- Cinema 4D
- 3dmax/ Maya
- Keyshot

## 3. 后处理

- Ps/ PPT (位图)
- Ai (矢量图)
- Pr/ Ae

## 4. 实验图绘制

- Origin
- Matlab
- python

## 5. 文档编辑与文献管理

- Office/ WPS
- Adobe Acrobat Reader DC
- Mendeley/ EndNote

## 6. 其他

- LabVIEW
- COMSOL
- Ansys



学汇百川 德济四海

A large cargo ship, identified by the text on its hull as '大连海事大学' (Dalian Maritime University), is shown sailing on a choppy blue sea under a clear sky. The ship has multiple decks and shipping containers stacked on its deck.

Thank You !